

Chemical bonding in transition metal carbonyl clusters: complementary analysis of theoretical and experimental electron densities.

Piero Macchi^{a,b,*}, Angelo Sironi^{a,b}

^a *Dipartimento di Chimica Strutturale e Stereochimica Inorganica, Università di Milano, Via Venezian 21, 20133 Milan, Italy*

^b *CNR-Istituto di Scienze e Tecnologie Molecolari, Via Golgi 19, Milan, Italy*

Received 4 March 2002; accepted 5 September 2002

Contents

Abstract	383
1. Introduction	384
2. Techniques	384
2.1 X-ray diffraction	384
2.2 Theoretical calculations	386
2.3 The atoms in molecules approach	387
3. Electron density analysis of transition metal carbonyl clusters	391
3.1 Carbonyl complexes	391
3.2 Dimeric compounds and the metal–metal bond	394
3.3 Carbonyl bridged and semibridged systems	397
3.3.1 Deformation density	401
3.3.2 Molecular graph	401
3.3.3 Laplacian distribution	401
3.3.4 Atomic charges	402
3.3.5 Bond indexes	402
3.3.6 Through bond versus through space interactions?	403
3.3.7 The complete structure diagram	404
3.4 Small clusters	404
3.5 Theory versus experiment	407
4. Toward a general understanding of metal–metal interactions	408
Acknowledgements	410
Appendix A	410
References	410

Abstract

In the last few years, the quantum theory of atoms in molecules has become the paradigm for interpreting theoretical and experimental electron density distributions. Within this framework, the link between bonding modes and topological properties has been fully achieved for ‘light atom’ molecules. However, the derived correspondence rules cannot be extended straightforwardly to organometallic compounds since bonds to a transition metal display a different and much narrower spectrum of topological indexes. The complementary usage of theoretical computations on a set of prototype transition metal molecules and experimental determinations of the electron density in transition metal carbonyl clusters are discussed. Since these compounds are characterised by weakly bound metal cages and fluxional carbonyl ligands, the focus is on the nature of metal–metal and metal–carbonyl interactions as well as on the evolution of three-centre-four-electron $M(\mu\text{-CO})M$ bonds along the $(\text{CO})M-M \leftrightarrow M(\mu\text{-CO})M \leftrightarrow M-$

* Corresponding author. Tel.: +39-02-5031-4451; fax: +39-02-5031-4454

E-mail addresses: piero@csmto.mi.cnr.it (P. Macchi), angelo@csmto.mi.cnr.it (A. Sironi).

M(CO) conversion path. The interpretation of the electron density distribution here proposed could be extended reasonably to a wider class of organometallic compounds.

© 2002 Elsevier Science B.V. All rights reserved.

Keywords: Transition metal carbonyl clusters; Electron density distribution; Accurate X-ray diffraction; Metal–metal bonds; Bridging carbonyl ligands

1. Introduction

As crystallographic techniques improved (1960s), it was soon put into practice [1] what had already been predicted in the early days of the scattering theory [2], i.e. that X-ray diffraction can be used for determining not only the geometry, but also the accurate electron density distribution of a molecule. The technique could give information on the chemical bonding and therefore compete with theoretical methods in depicting models. The X–N deformation maps were, in fact, a tool comparable to theoretical deformation densities. The first applications dealt with small organic molecules, though the extension to organometallic and inorganic complexes occurred quite early [3], despite the inherent difficulty of dealing with heavy atoms (whose diffraction pattern is dominated by core electrons, almost perfectly spherical and ineffective in the chemical bonding).

More recently (1990s), the advent of new and faster technologies (especially the area detectors) represented a second breakthrough in this field. In fact, studies on larger systems, even polymetal compounds, have appeared, given that data collections have become much faster and large unit cell crystals are no longer unaffordable. At the same time, the quality of the collected data has also improved, giving more confidence and accuracy to the results [4].

The great improvement in experimental methods paralleled those in the theoretical field, where progress in either computer science and new theoretical methodologies (especially the gradient-corrected density functional theory) made studies on medium-large organometallic systems affordable [5]. In addition, comparisons between theory and experiment have been simplified since a common approach to analyse the total electron density (the quantum theory of atoms in molecules, QTAM [6]) has been routinely applied.

During the last 30 years, Bader and co-workers have demonstrated that the analysis of $\rho(\mathbf{r})$ topology is as easily understandable as the qualitative molecular orbital (MO) models, with two advantages: a more quantitative consistency (because $\rho(\mathbf{r})$ can be obtained with very accurate methods,¹ some of which, however,

may lack straightforward interpretation in MO terms²) and a robust physical basis (because $\rho(\mathbf{r})$ is an observable, at variance from atomic or molecular orbitals).

Thorough QTAM analysis of many main group light atom molecules has led to the identification of a set of ‘correspondence rules’ between common chemical concepts and topological properties of the electron density. However, such an analogy cannot be easily extended to organometallic compounds, which have an inherently different ‘physics’ due to the overwhelming presence of donor–acceptor bonds and to the character of the orbitals involved, with the simultaneous presence of diffuse ns and contracted $(n-1)d$ electrons. Many recent studies have indicated that bonds to a transition metal display a different and much narrower spectrum of topological indexes, though a comprehensive rationalisation is still missing. In addition, the nature of the metal–metal bond is not completely understood yet and much debate is still occurring on its actual presence, role and mechanism.

The aim of this review is providing a rationale for the observed electron density distribution in transition metal carbonyl dimers and low nuclearity clusters, with a special focus on the nature of the metal–metal bond within the cages and on the influence of terminal and bridging CO ligands.

2. Techniques

2.1. X-ray diffraction

In the kinematic approximation, the intensity diffracted by a plane of a single crystal is proportional to the square of the structure factor modulus:

$$I \propto |F|^2 \quad (1)$$

Bragg intensities are obtained from experimental integrated reflectivities corrected for absorption, extinction, thermal diffuse scattering, multiple scattering and beam/crystal decay. The Bragg structure factors are Fourier transforms of the thermally smeared electron density of the unit cell in the crystal:

¹ We include in the list of methods to obtain $\rho(\mathbf{r})$ also refinements of density matrixes, wave functions or multipolar expansion coefficients against experimental data. Depending on the quality of the measured data, these methods can be considered among the most accurate ones, vide infra.

² This is necessarily true for multipolar expansions of the electron density as well as for multi-reference methods.

$$F(\mathbf{S}) = \int \rho(\mathbf{r}) \exp(2\pi i \mathbf{S} \cdot \mathbf{r}) d\mathbf{r} \quad (2)$$

where \mathbf{S} is a vector in the reciprocal lattice of the crystal. Within a pseudo-atomic approximation, the structure factor depends on the atomic form factors, mean positions and mean-square displacements:

$$F(\mathbf{S}) = \sum_i f_i(\mathbf{S}) \exp(2\pi i \mathbf{S} \cdot \mathbf{r}_i) T_i(\mathbf{S}) \quad (3)$$

where $T_i(\mathbf{S})$ is the thermal vibration factor. Thus, the mean thermal electron density in the unit cell could be calculated by inverse Fourier summation over the reciprocal lattice vectors \mathbf{S} , of the X-ray crystal structure factors:

$$\rho(\mathbf{r}) = \frac{1}{V} \sum_{\mathbf{S}} F(\mathbf{S}) \exp(-2\pi i \mathbf{S} \cdot \mathbf{r}_p) \quad (4)$$

Due to termination of the series, $\rho(\mathbf{r})$ is always severely affected by ripples and cannot be used for mapping the total electron density. Difference functions $\Delta\rho(\mathbf{r})$, instead, are less sensitive to termination because the ripples are mutually cancelled by the subtraction:

$$\begin{aligned} \Delta\rho(\mathbf{r}) &= \rho(\mathbf{r})^{\text{obs}} - \rho(\mathbf{r})^{\text{cal}} \\ &= \frac{1}{V} \sum_{\mathbf{S}} (F(\mathbf{S})^{\text{obs}} - F(\mathbf{S})^{\text{cal}}) \exp(-2\pi i \mathbf{S} \cdot \mathbf{r}) \end{aligned} \quad (5)$$

$\rho(\mathbf{r})^{\text{cal}}$ is the electron density of a reference system, which typically is the simple superposition of independent, spherical atoms vibrating at their unit cell positions (promolecule). A map obtained with the Fourier summation (5) is called the experimental deformation density [7]. In order to enhance the features of chemical bonding, the map can be ‘cleaned’ by including in the summation only the shorter scattering vectors, which contain most of the diffraction from valence (diffuse) electrons.

The main drawback of the deformation density approach is the same of its theoretical analogue: the information depends on the reference model, which is especially crucial if the atomic ground state is degenerate [8] or the electronic configuration of the isolated atom is different from that of the atom in the molecule.³ This significantly affects a deformation density when the total density between two covalently bonded atoms is small or when the two atoms have more than half-filled shells (for example F–F bonds in F_2 molecule, but also C–F and O–O bonds [9]). The problem could be solved only by introducing the so-called chemical deformation densities [10], where the promolecule is produced using ad-hoc atomic hybridisation. Additional uncertainties are caused by improper deconvolution of the thermal

motion, which may bias the chemical bonding features. To overcome this problem, one can use unbiased positional and thermal parameters, obtained from a separate neutron diffraction experiment (X–N deformation density) [11], although this requires more experimental efforts.

A dramatic improvement in the experimental electron density modelling came by the development of methods to describe the aspherical components of the atomic $\rho(\mathbf{r})$ [12]. The most commonly used approach is a multipolar expansion of atom centred densities [12a]:

$$\rho(\mathbf{r}) = \sum_{\text{atoms}} \rho_i(\mathbf{r} - \mathbf{r}_i) \quad (6)$$

$$\begin{aligned} \rho_i(\mathbf{r}) &= P_{i,\text{core}} \rho_{i,\text{core}}(\mathbf{r}) + \kappa^3 P_{i,\text{val}} \rho_{i,\text{val}}(\kappa \mathbf{r}) \\ &+ \sum_{l=0}^{l_{\text{max}}} \left[\kappa'^3 R_l(\kappa' \mathbf{r}) \sum_{m=0}^l P_{ilm\pm} y_{lm\pm}(\mathbf{r}/r) \right] \end{aligned} \quad (7)$$

The multipole expansions are normally terminated at $l_{\text{max}} = 4$. Transforming Eq. (7) in the reciprocal space and adopting a least-square procedure, the population coefficients P_{ilm} and the radial scaling κ and κ' become additional variables, to be refined together with positional and thermal parameters. The advantages of this method are the more accurately refined thermal parameters (which typically become very close to neutron diffraction estimations [13]) and the possibility of reconstructing in direct space, without ripples and thermal smearing, $\rho(\mathbf{r})$ as well as many derived properties (static $\Delta\rho(\mathbf{r})$, Laplacian, electrostatic potential, etc.). An important task is the choice of the radial description for the density. ρ_{core} and ρ_{val} are typically constructed from atomic wave functions obtained at Hartree–Fock (HF) [14] level or from wave functions fitted to reproduce Dirac–Fock (DF) atomic densities [15]. The radial part of the multipolar expansion is taken either from the best single- ζ exponents [16] for the valence shell or from HF or DF expansion of valence orbitals. The latter procedure is suggested for transition metal compounds, where the shape of the atomic d-density is substantially preserved in the molecular context [17], due to the contraction of d orbitals.

A partitioning of d-electrons was introduced by Holladay et al. [18], and it has been widely employed whenever transition metal atom complexes have been studied. Under the approximation of low overlap with the ligands, the electron density ρ_d produced by d_i orbitals can be expressed as:

$$\rho_d = \sum_{i=1}^5 P_i d_i^2 + \sum_{i=1}^5 \sum_{j>i}^5 P_{ij} d_i d_j \quad (8)$$

where $d_i = R_d(\mathbf{r}) y_{lm\pm}(\mathbf{r}_d(\mathbf{r}))$ being the radial part of a metal d orbital). If we consider metal d-electrons only, expansion (7) can be reduced and equated to Eq. (8). Because both expressions use spherical harmonics

³ For example, C in isolation is $s^2 p^2$ (which is also a degenerate state) while a sp^3 hybridisation is very usual.

(which are a complete set of functions), we can write a matrix relation between multipolar ($P_{lm\pm}$) and orbital (P_i) populations:

$$\mathbf{P}_{lm\pm} = \mathbf{M}\mathbf{P}_i \quad (9)$$

The matrix \mathbf{M} is constructed using the decomposition of spherical harmonic products and the tabulated normalisation constants [19]. The inverse matrix \mathbf{M}^{-1} allows calculations of orbital populations from the refined multipolar coefficients.

Many experimental requirements are necessary for an accurate determination of the electron density distribution. Because multipolar refinements use more parameters than conventional spherical atom refinements, more intensities have to be measured to grant an observation/variables ratio of at least 10. In addition, in order to reduce correlation among variables, high order data are particularly important to determine thermal parameters (because valence electrons have negligible scattering at high diffraction angles). The resolution limit, however, depends on the atomic composition, as in fact heavy atoms have significant scattering at larger diffraction angles. Moreover, transition elements have rather contracted $(n-1)d$ valence orbitals, whose scattering is therefore quite important even at $\sin \theta/\lambda = 0.7 \text{ \AA}^{-1}$. The way to increase high order diffraction is that of reducing the thermal motion by lowering the temperature of the crystal. The most commonly employed equipment make use of liquid N_2 or He as coolant, giving temperatures about 100 K or below 20 K, respectively. For practical reasons, low temperature apparatus with open flow N_2 stream are the most commonly employed, though, of course, the lower is the temperature the more accurate is the result. Lowering the temperature affords some additional benefit [20]: (a) the reduced thermal motion quenches the correlation between thermal and density parameters; (b) the anharmonic components of the atomic motion is smaller, resulting in a simplified tensor; (c) the thermal diffuse scattering is significantly reduced; (d) chemical instability or radiation damage of the crystal is reduced.

Since accuracy and precision in the measurements are mandatory, data collections are typically quite slow and intensities are repeatedly measured. In this context, much progress was induced by the area-detector technology, which drastically reduced data collection times. Further accuracy can be obtained also by using synchrotron radiation as X-ray source, because the intensity is many order of magnitude larger and the wavelength is tuneable. This allows the selection of a smaller specimen and an appropriate wavelength to significantly reduce extinction and absorption.

As we anticipated, studies on compounds containing heavy atoms have an inherent loss in accuracy, given the quite large number of core electrons in diffraction. This problem was ‘quantified’ by the so-called suitability

index [21]:

$$s = V_{\text{cell}} \cdot \left(\sum_j n_{f,\text{core}}^2 \right)^{-1} \quad (10)$$

Organic molecular crystals generally have $s > 1.0$, while transition metal complexes have smaller s . When this index was first introduced, compounds with suitability less than 1.0 were considered at the limits of the available accuracy. The technological improvements occurred in the last 20 years allow us to state that studies with $s < 0.5$ are presently affordable and the current limit is probably $s \sim 0.1$. This means that polymetal compounds of the first transition row and mononuclear complexes of the second transition are suitable study objects, while the current new frontier is represented by third row complexes or the high nuclearity clusters.

Many recent reviews [4] and books [22] describe in detail all the aspects of accurate experimental crystallography and electron density determinations. The reader is referred to these references for further information and for a wide presentation of the available software.

If not otherwise mentioned, the experiments reported in this paper have been performed in our laboratory, using a SMART-CCD diffractometer equipped with a N_2 flow low temperature device. Refinements were carried with a modified version [23]⁴ of the XD package [24]. Further details on the data collection, corrections to measured intensities and refinement procedures have been reported in dedicated papers or will be described in forthcoming publications.

2.2. Theoretical calculations

Other articles in this issue are concerned with the methodological improvements of quantum chemical calculations in transition metal chemistry. We can briefly mention that progress in the last decade is certainly due to gradient-corrected density functional theory (GGA and hybrid functionals) and small-core relativistic effective core potentials. Optimised geometries and calculated energies (as well as many other properties) are typically in very good agreement with the experimental results, with costs comparable to those of HF calculations. Consequently, this has favoured also

⁴ The XD code was extended to include atoms beyond the first transition and to use relativistic wave functions. A few errors in the calculations of the properties were found and corrected. Some of these however affected previous results reported by us. We report in this review new (correct) results based on the same models deposited in Refs. [70,85]. In particular, the deformation of metal 3d shells in the Laplacian distribution was underestimated, see Fig. 8. Luckily, the electron density topologies are not qualitatively affected and all the parameters at the bcp's are not significantly different.

Table 1

Main features of the electron density distribution in some prototype bonding interactions, calculated at QCISD/ae level

Bond	d_{A-bcp} (Å)	d_{B-bcp} (Å)	$\rho(\mathbf{r}_{bcp})$ (e Å ⁻³)	$\nabla^2\rho(\mathbf{r}_{bcp})$ (e Å ⁻⁵)	$H(\mathbf{r}_{bcp})/\rho(\mathbf{r}_{bcp})$ (he ⁻¹)	$G(\mathbf{r}_{bcp})/\rho(\mathbf{r}_{bcp})$ (he ⁻¹)	$\int_{A\cap B}\rho(\mathbf{r})$ (e Å ⁻¹)	$\delta(A,B)$ [SCF]	Mayer BO
H–H	0.372	0.372	1.750	–24.71	–1.028	0.040	1.42	1.00	1.00
H ₃ C–CH ₃	0.766	0.766	1.623	–13.64	–0.844	0.256	2.16	1.01	0.80
H ₂ C=CH ₂	0.670	0.670	2.262	–23.83	–1.159	0.421	2.94	1.90	1.96
HC≡CH	0.605	0.605	2.659	–27.10	–1.425	0.711	3.70	2.85	3.67
H ₃ C–OCH ₃	0.481	0.933	1.744	–9.94	–1.401	1.002	2.32	0.90	0.90
H ₂ C=O	0.412	0.799	2.755	–1.40	–1.680	1.644	3.03	1.58	2.16
C≡O	0.383	0.751	3.194	20.29	–1.759	2.203	3.17	1.80	2.21
Na–F	0.923	1.063	0.292	8.63	0.288	1.785	0.46	0.27	0.33
Ne–Ne	1.577	1.577	0.012	0.36	0.593	1.514	0.02	0.002	0.01
Na–Na	1.582	1.582	0.055	–0.06	–0.160	0.080	0.50	1.00	1.00
K–K	1.990	1.990	0.032	0.03	–0.071	0.140	0.42	0.82	0.99

The delocalisation index is based on the SCF density (computed on the QCISD/ae optimised geometry).

the analysis of the electron density distribution, which is of course very sensitive to the molecular geometry.

The absence of core electrons in effective core potential basis sets may affect an accurate topological investigation, especially if dealing with weak bonds. To overcome this problem, one can add a posteriori the core-electron density[25] or produce a single-point calculation with an all-electron basis set on the optimised geometry.

If not otherwise mentioned, the geometry optimisation and single point calculations here reported are performed with the GAUSSIAN98 [26] package at the DFT level of theory, using the hybrid B3LYP [27] functional. The basis set employed are: (1) ecp: small-core relativistic effective core potentials [28] with basis set splitting (341/311/41) for the 1st transition metals and double zeta quality [29] all-electron basis (721/41) augmented with two d functions for second row atoms; (2) ae: all electron basis set of 6-311++G with d and f polarisation functions for the main group atoms and transition metals, respectively [30]. The prototype molecules of the main group atoms reported in Table 1, were calculated with the ae basis set and quadratic configuration interaction using single and double excitations (QCISD) of the HF-SCF ground state (similar results were obtained with DFT). Some bonding analyses have been performed with routines implemented in GAUSSIAN98 or external codes, such as MAYER [31] (to compute bond orders).

2.3. The atoms in molecules approach

As shown by Bader and co-workers, important chemical information can be retrieved from the total electron density distribution of a molecule. A topological analysis is the search of critical points of the three-dimensional function $\rho(\mathbf{r})$, which occur when the gradient $\nabla\rho(\mathbf{r})$ vanishes. The critical points are classified

based on the rank⁵ and the signature⁶ of the related Hessian matrix. Local maxima of the density, labelled as (3,–3) critical points, are found in nuclear positions [32].⁷

The total electron density can be uniquely partitioned, assigning to each local maximum a volume of the space (basin) delimited by zero flux surfaces. Therefore, an atom can be characterised by the union of a local (nuclear) maximum and the corresponding basin (atomic basin). Integration of $\rho(\mathbf{r})$ over this volume gives atomic populations and therefore charges, Q .

A chemical bond between two atoms is characterised by a line of maximum electron density (the bond path, bp) which links the two atomic nuclei and intersects a zero-flux surface (interatomic surface) at a (3,–1) saddle critical point (the bond critical point, bcp). Based on these definitions, a chemical structure is simply the topological graph produced by the bond paths and the maxima of the density. Some structures necessarily contain other critical points of the density: the (3,+1) type is characteristic of rings (ring critical point, rcp) while the (3,+3) type (a local minimum) is produced inside cages (cage critical point, ccp). The total number and type of non-degenerate critical points is determined by the Poincaré–Hopf relation [33] in a molecule and by the Morse equation [34] in a crystal.

The shape of the bond path or the deformation from cylindrical symmetry along it are often important indicators of the bond nature. For example, non-straight bond paths characterise the so called bent

⁵ Number of non-zero eigenvalues λ_i .

⁶ Sum of the sign of the eigenvalues.

⁷ Additional maxima of $\rho(\mathbf{r})$ have been found at non-nuclear positions in some bulk metals or metal clusters, see Ref. [32]. Much debate is still in due course about the meaning of this feature (which sometime is found to be an ambiguity of the model used to compute the electron density).

bonds (as C–C in *cyclo*-propane), while the presence of π -density leave traces in the ellipticity ε of the bond⁸ because it produces a preferential plane of accumulation for the charge density.

The idea of bond path is sometime erroneously confused with the Lewis bond, and consequently the molecular graph with the Lewis structure [35].⁹ A few warnings are important for interpretative purposes. A bond path does not contain in itself information on the number of electrons associated with the corresponding bond. In fact, a bond path is found between the two noble gases in a van der Waals dimer (often defined through the oxymoron ‘non-bonded molecule’) as well as between the two hydrogens in H₂. Moreover, electron delocalisation, although stabilising, does not afford bond paths between ‘far’ atoms: in allylic systems, for instance, the terminal carbons are not linked by a bond path, although π valence electrons are actually shared among all three atoms. As we will see in the following, traditional bonding concepts can be retrieved instead by analysing many features of the electron density along the bond path, on the interatomic surface and in the atomic basins. In fact, atomic interactions leave precise fingerprints, quite representative of the nature itself of the chemical bond.

In Table 1, some prototype bonds are reported and the main features of homopolar covalent, heteropolar, ionic and van der Waals bonds are shown. A first important indicator is the electron density at the bcp, $\rho(\mathbf{r}_{\text{bcp}})$, which can be related to the bond order, though only within homogeneous series. In fact, bonds between atoms with diffuse valence electrons tend to have smaller $\rho(\mathbf{r}_{\text{bcp}})$. The electron density integrated over the whole interatomic surface ($\oint_{A \cap B} \rho(\mathbf{r})$) provides an alternative and more informative index. On the other hand, interactions between almost purely spherical atoms with negligible electron sharing (such as noble gases) are characterised by a small $\rho(\mathbf{r}_{\text{bcp}})$ and a small $\oint_{A \cap B} \rho(\mathbf{r})$.

A very useful source of information is the analysis of the Laplacian of the electron density, $\nabla^2 \rho(\mathbf{r})$, which enhances features of charge distribution and of electron pair localisation, providing a physical connection with the classical Lewis model and the valence shell electron pair repulsion theory (VSEPR) [36]. $\nabla^2 \rho(\mathbf{r})$ addresses the regions of charge concentrations ($\nabla^2 \rho(\mathbf{r}) < 0$) and those of charge depletion ($\nabla^2 \rho(\mathbf{r}) > 0$). As pointed out by Bader and co-workers [37], the function $-\nabla^2 \rho(\mathbf{r})$ of

an isolated ground state atom¹⁰ define a density shell structure that has a one-to-one correspondence with the electronic shell structure [38].¹¹ However, for heavy atoms this correspondence is lost [39]: fourth row elements, from Sc to Ge, do not show the expected maxima and minima of the N shell (which is thus not distinguishable from the M shell) but, starting from As (up to Kr), M and N shells are again separated even if the outermost maxima do not necessarily have $-\nabla^2 \rho(\mathbf{r}) > 0$ (see Fig. 1a). Similar trends occur to elements of the successive rows¹² and have been imputed to the diffuse character of the outermost electrons when the atomic core is large.

When a chemical bond is formed the atomic Laplacian distribution is no longer spherical and its properties are widely used for characterising atomic interactions. When two second row atoms are covalently bonded, two maxima of $-\nabla^2 \rho(\mathbf{r})$,¹³ called valence shell charge concentrations (VSCC), are found along the bond path, one for each atomic basin. The outermost shells of the two bonded atoms partially overlap before concluding the termination of the shell-structure shape, thus at the bcp $\nabla^2 \rho(\mathbf{r}) < 0$ (Fig. 1b). Therefore, it is quite reasonable to take the value of $\nabla^2 \rho(\mathbf{r}_{\text{bcp}})$ for characterising strength and degree of covalency of an homopolar interaction between two light atoms.

If instead we consider the electron density distribution of a noble-gas dimer, we note that no overlap between the two shells is actually occurring, and the bcp lies in a region produced by the outermost shell closure of both atoms (Fig. 1b). Therefore, $\nabla^2 \rho(\mathbf{r}_{\text{bcp}})$ is positive here and it perfectly represents the tendency to contract the charge away from the interatomic surface toward the inner part of the atomic basin. Indeed, $\rho(\mathbf{r}_{\text{bcp}})$ and $\oint_{A \cap B} \rho(\mathbf{r})$ are both very small.

When the bond is ionic, like in NaF, the outermost shell of the cation is captured by the anionic basin and, along the bond path, one cannot totally distinguish the

¹⁰ Based on the Clementi and Roetti HF wave functions (Ref. [14]).

¹¹ The actual physical meaning of this feature has been widely discussed in the past few years; however, it has been demonstrated that none of the critical point of $-\nabla^2 \rho(\mathbf{r})$ (minima and maxima) nor the zeros can reproduce the expected number of electrons within a given shell (see Ref. [38a]). Thus, $-\nabla^2 \rho(\mathbf{r})$ is a better qualitative index of atomic shells occurrence (as respect to the radial density distribution, $D(r)$, which also lacks of local maxima for the outermost shells), but is a worse quantitative index (see for comparison Ref. [38b]). The lack of outermost shells for heaviest elements occurs also in the Laplacian of the conditional pair density, which has been shown to exhibit a (topological) structure diagram, homeomorphic with the Laplacian of the density when the reference pair is strongly localised, see Ref. [38c].

¹² The maximum number of distinguishable shells is five (see Ref. [39a]).

¹³ Formally, a VSCC is found when a $-\nabla^2 \rho(\mathbf{r})$ maximum occur with $\nabla^2 \rho(\mathbf{r}) < 0$.

⁸ $\varepsilon = \lambda_1/\lambda_2 - 1$ (λ_1, λ_2 are the two negative eigenvalues of the Hessian matrix, with $\lambda_1 \geq \lambda_2$).

⁹ ‘The use of a bond path to denote a bonded interaction frees the definition of bonding from the constraints of the Lewis electron pair model, a model that is unable to describe the bonding in metals and in condensed phases composed of closed shell atoms or neutral or charged molecules’ (from Ref. [35]).

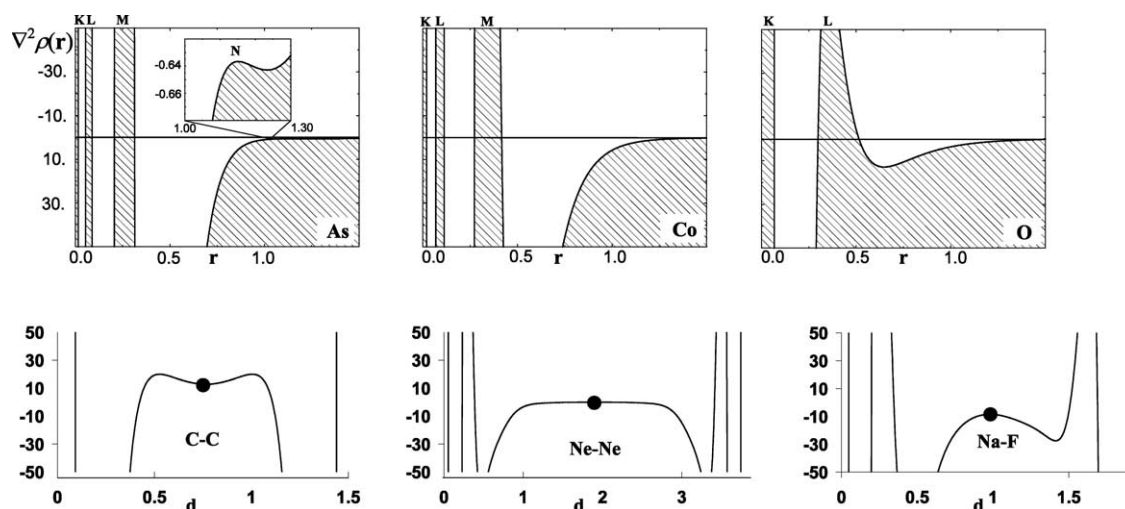


Fig. 1. Top: profile of the Laplacian distribution of the spherically averaged density for As, Co and O atoms; note the lack of the N shell (4s) for Co and the ‘hidden’ maximum for As. Bottom: profile of the Laplacian distribution (at B3LYP/ae level) along the C–C, Ne–Ne and Na–F bond paths in C_2H_6 , Ne_2 and NaF molecules; the bcp’s are represented as filled circles. Distances are in Å, Laplacian in $e \text{ Å}^{-5}$.

M shell of Na which is partially ‘hidden’ by the L shell of F. The bcp is shifted towards Na, and it lies in a flat region of the Laplacian, with $\nabla^2\rho(\mathbf{r}_{\text{bcp}}) > 0$. The situation is similar to that of Ne–Ne, apart for the obvious charge transfer and the tendency to have larger $\rho(\mathbf{r}_{\text{bcp}})$ and $\phi_{A \cap B}(\mathbf{r})$ due to small covalent contribution.

Depending on the degree of polarity, heteropolar bonds display features closer to one or the other prototype. The atomic basin of the more electronegative element overwhelms and the interatomic surface is shifted toward the more electropositive atom [40]. It may occur that the bcp lie close to the nodal surface of the Laplacian with both VSCC’s belonging to more electronegative basin, as for carbon monoxide. Here, $\nabla^2\rho(\mathbf{r}_{\text{bcp}})$ is not particularly indicative because small geometrical distortions may significantly change its value and even its sign. The shift of bcp toward the electropositive atom may not be evident if the atoms have significantly different atomic radii (as for interactions between metals and organic ligands). To overcome this problem, a useful indicator (the non polar midpoint [41]¹⁴) was introduced for scaling the bcp location according to the actual atomic sizes.

At each point \mathbf{r} , a local virial theorem [6] links the Laplacian of the electron density to two important quantities, the kinetic energy density $G(\mathbf{r})$ (everywhere positive) and the potential energy density $V(\mathbf{r})$ (everywhere negative). In covalent bonds, $V(\mathbf{r})$ is dominating, thus the total energy density ($H(\mathbf{r}) = G(\mathbf{r}) + V(\mathbf{r})$) is

negative at the bcp [42].¹⁵ On the other hand, excess of kinetic energy density is related to Pauli repulsion between two closed shells, as it occurs for example on the interatomic surface separating two noble gases or ions, where in fact $H(\mathbf{r}_{\text{bcp}}) > 0$ and $G(\mathbf{r}_{\text{bcp}})/\rho(\mathbf{r}_{\text{bcp}}) > 1$. The $G(\mathbf{r}_{\text{bcp}})/\rho(\mathbf{r}_{\text{bcp}})$ ratio increases as the interatomic surface lies closer to an atomic core, thus it grows with the bond order in homopolar interactions due to the smaller internuclear separations (see for example the series C–C, C=C and C≡C in Table 1). Analogously, $G(\mathbf{r}_{\text{bcp}})/\rho(\mathbf{r}_{\text{bcp}})$ is large in polar interactions because the interatomic surface is particularly penetrated into the atomic core of the electropositive atom.

Going beyond an electron density distribution analysis, Bader and Stephens proposed a partitioning of the pair density distribution in order to define a localisation index (number of electron pairs localised inside an atomic basin) and a delocalisation index (number of

¹⁵ As demonstrated in Ref. [42a] the sign of the energy density computed at the bcp is an index of the amount of covalency in the chemical interaction.

¹⁶ Pairing of electrons is a consequence of the Pauli exclusion principle and its spatial localisation is determined by the corresponding property of the density of the Fermi hole. The average number of pairs in the atomic basin A and that in common between atoms A and B are: $D_2(A, A) = \int_A d\mathbf{r}_1 \int_A d\mathbf{r}_2 \rho(\mathbf{r}_1, \mathbf{r}_2) = [N(A)^2 + F(A, A)]/2$; $D_2(A, B) = \int_A d\mathbf{r}_1 \int_B d\mathbf{r}_2 \rho(\mathbf{r}_1, \mathbf{r}_2) = [N(A)N(B) + F(A, B)]/2$ where $\rho(\mathbf{r}_1, \mathbf{r}_2)$ is the pair distribution function; $N(A)$ and $N(B)$ are the total electron density integrated over the atomic basins A and B, respectively; $F(A, A)$ and $F(A, B)$ are the total Fermi correlations contained within and atomic basin or shared between two basins, respectively. At the Hartree–Fock level of theory, where the Fermi hole is the sole source of electron correlation, $F(A, A)$ and $F(A, B)$ reduce to: $F(A, A) = -\sum_i \sum_j S_{ij}(A)^2$ and $F(A, B) = F(B, A) = -\sum_i \sum_j S_{ij}(A)S_{ij}(B)$ where $S_{ij}(A)$ is the overlap integral $\langle \phi_i | \phi_j \rangle_A$ over the atomic basin A. The quantity $\delta(A, B) = F(A, B) + F(B, A)$ is called delocalization index and represents a measure of the total Fermi correlation shared between the atoms or, in other words, the number of shared electrons.

¹⁴ For a A_1 – A_2 bond we can evaluate $m_1 = r_1 r_{12} (r_1 + r_2)^{-1}$, which is the distance of the nonpolar midpoint from atom A_1 , r_1 and r_2 are the covalent radii of A_1 and A_2 , respectively, r_{12} is A_1 – A_2 bond distance.

electron pairs delocalised between two atoms, hereinafter $\delta(A,B)$ [43].¹⁶ At the HF level of theory, $\delta(A,B)$ are in almost exact agreement with the Lewis theory, while correlated calculations show some significant reduction of the bonded electron pairs compared to the expectations of electron counting rules [44]. Due to the reduced covalency, polar bonds have a $\delta(A,B)$ smaller than the predicted bond order (Table 1). Eventually, ionic bonds have very small $\delta(A,B)$, though some residual electron sharing persists, again due to small covalent ‘contamination’ of a purely closed-shell form. Noble gas interactions have almost zero $\delta(A,B)$, in agreement with the bond order.¹⁷ Recently, $\delta(A,B)$ indexes were used for characterising interactions with significant delocalisation [45]. In fact, $\delta(A,B)$ is not restricted to atoms sharing a common interatomic surface and therefore is an indicator able to depict the ‘electronic communication’ between atoms. As we mentioned above, the information about electron delocalisation between atoms that are not directly linked through a bond path can not be contained in the features of the other bond paths (apart for their curvature that can be indicative in some cases, as we will see below).

Due to the ‘anomalous’ behaviour shown by heavier elements, some of the features described so far for characterising chemical interactions undergo significant ‘tuning’ on descending the periodic table. Indeed, charge concentrations along the bond path become weaker, as demonstrated by $\rho(\mathbf{r}_{\text{bcp}})$, $\oint_{A \cap B} \rho(\mathbf{r})$ and $\nabla^2 \rho(\mathbf{r}_{\text{bcp}})$ in the homologous series H_2 , Na_2 , K_2 . At the same time the ratio $\oint_{A \cap B} \rho(\mathbf{r})/\rho(\mathbf{r}_{\text{bcp}})$ increases with the diffuse character of the electrons involved in the bonding. Nevertheless, the delocalisation index is almost constant and reproduces the bond order expected from simple MO theory. Other features preserved on descending a group are the negative value of $H(\mathbf{r}_{\text{bcp}})$ (whose absolute amount however decreases) and the small amount of kinetic energy density, measured by $G(\mathbf{r}_{\text{bcp}})/\rho(\mathbf{r}_{\text{bcp}})$. Accordingly, we can better distinguish between the indexes linked to a given bonding mechanism and those linked to the strength of the interaction. Thus, covalency is represented by a dominant potential energy density (hence $H(\mathbf{r}_{\text{bcp}}) < 0$), a small kinetic energy density in relative terms ($G(\mathbf{r}_{\text{bcp}})/\rho(\mathbf{r}_{\text{bcp}}) < 1$) and a delocalisation of some electron pairs between the atoms ($\delta(A,B) \sim$ bond order). The strength of a covalent bond is measured by the amount of electron density ($\rho(\mathbf{r}_{\text{bcp}})$, $\oint_{A \cap B} \rho(\mathbf{r})$) and the degree of concentration ($\nabla^2 \rho(\mathbf{r}_{\text{bcp}})$).

¹⁷ All atomic interactions involve some degree of pairing of the electrons on the two atoms, even interactions between noble gases, that, using correlated wave functions, exhibit small values of $\delta(A,B)$, which increase with the size and polarizability of the atoms involved (see ref. [57]).

On the other hand, closed-shell interactions are dominated by excess of kinetic energy density ($G(\mathbf{r}_{\text{bcp}})/\rho(\mathbf{r}_{\text{bcp}}) > 1$; $H(\mathbf{r}_{\text{bcp}}) > 0$), small electron density concentration ($\nabla^2 \rho(\mathbf{r}_{\text{bcp}}) > 0$); small $\oint_{A \cap B} \rho(\mathbf{r})$ and $\rho(\mathbf{r}_{\text{bcp}})$ and negligible electron sharing ($\delta(A,B) \sim 0$).

Some authors have proposed a formal separation between open shell and closed shell interactions based on the sign of $\nabla^2 \rho(\mathbf{r}_{\text{bcp}})$ only [46]. Although any classification is always in principle acceptable, we note that this proposal would lack of a strict relation with the concepts already in use in the chemical community and that it could not exhaust the vast variety of chemical bond types known, as demonstrated by the countless ‘exceptions’. In this respect, we will later discuss two major cases, namely polar-shared interactions, such as found in CO (see Section 3.1), and bonding between and with transition metals (see Sections 3.1 and 3.2). A different classification, giving responses closer to the chemical sense, was proposed by Cremer and Kraka [42,47], who suggested the fulfilment of two conditions to define a covalent bonding: (a) the presence of a bond path linking the two atoms; and (b) an overwhelming potential energy density at the bcp ($H(\mathbf{r}_{\text{bcp}}) < 0$). Instead, Bader, the founder and the most careful investigator of the physics behind QTAM, has always used an inductive approach to derive the ‘correspondence rules’ between fuzzy chemical insight and precise topological entities [6]. Indeed, he never formulated a formal classification based only on $\nabla^2 \rho(\mathbf{r}_{\text{bcp}})$ (nor on $H(\mathbf{r}_{\text{b}})$), although he noted a tight connection between the sign of the Laplacian and the nature of the bond in most of the main group light atom molecules he studied. Inductively derived ‘correspondence rules’ clearly depend from the set of bonding types used in their formulation, accordingly, they must be tuned whenever new bond types are considered; Bader’s reasoning on Ga–Ga multiple bonds is quite relevant in this respect [48].

All the properties of $\rho(\mathbf{r})$ are available from both a theoretical and an experimental determination, although energy densities and delocalisation indexes can be exactly computed only knowing the wave function. Abramov proposed a functional [49]¹⁸ which relates the electron density and its derivatives to the kinetic energy density $G(\mathbf{r})$, valid at least in the regions of moderate overlap. Thus, $G(\mathbf{r})$ and (through the local

¹⁸ The kinetic energy density at the bond critical point is estimated by: $G(\mathbf{r}_{\text{b}}) = (3/10)(3\pi^2)^{2/3} \rho(\mathbf{r}_{\text{b}})^{5/3} + 1/6 \nabla^2 \rho(\mathbf{r}_{\text{b}})$ (1) (all quantities must be expressed in atomic units). For interactions dominated by large orbital overlapping the best approximation is: $G(\mathbf{r}_{\text{b}}) = (3/10)(3\pi^2)^{2/3} (\Delta \rho(\mathbf{r}_{\text{b}})^{5/3} + \rho_{\text{hyb}}(\mathbf{r}_{\text{b}})^{5/3}) + 1/6 \nabla^2 \rho(\mathbf{r}_{\text{b}})$ (2), where $\Delta \rho(\mathbf{r}_{\text{b}})$ and $\rho_{\text{hyb}}(\mathbf{r}_{\text{b}})$ are obtained by taking into account a proper promolecule which depends on the atomic hybridization; of course, when the asphericity of the total density is rather small Eq. (2) is equivalent to Eq. (1).

virial theorem) $V(\mathbf{r})$ and $H(\mathbf{r})$ are empirically estimable also experimentally [50].

The programs used for QTAM analysis are AIMPAC [51], AIM2000 [52], MORPHY98 [53] and WBADER [54] for theoretical electron densities and XD [23,24] for experimental electron densities.

3. Electron density analysis of transition metal carbonyl clusters

3.1. Carbonyl complexes

Transition metal carbonyl complexes were among the first examples of inorganic compounds studied through accurate X-ray mapping of the electron density. For example, in 1973 Rees and Coppens [3a] performed an X–N analysis on $\text{Cr}(\text{CO})_3(\text{C}_6\text{H}_6)$ showing the features of metal–carbonyl bonds: the CO lone pair density of the ligand is slightly polarised toward the metal, but the ‘charge center’ remains close to the carbon atom; the metal atom is surrounded by the peaks of the d orbitals disposed according to the ligand field theory (LFT) prediction. A few years later, Rees and Mitschler [55] gave more quantitative details on $\text{Cr}(\text{CO})_6$, computing atomic charges and quantifying the σ -donation and π -back donation effects, that were estimated similar in extent. Recent and accurate theoretical calculations [5b] with appropriate energy breakdown speak for a more relevant contribution of back-donation to the stabilising energy (a feature however that is not recoverable by a simple charge partitioning). Nevertheless, the experiment by Rees and Mitschler showed that studies on transition metal complexes could be carried, at least at a qualitative level. In fact, to that date, just one SCF and a few semi-empirical calculations on $\text{Cr}(\text{CO})_6$ were known,¹⁹ though without reaching any agreement in estimated atomic charges and orbital occupancies.

Some polymetal carbonyl compounds were also investigated by low temperature X-ray crystallography. While more attention was paid to presence (or absence) of some metal–metal bonding (see the discussion below), the features already revealed in the previous experiments were confirmed. Most of these early studies were afterwards re-examined by Holladay et al. [18] testing the method to extract d occupancies from multipole populations (see Eq. (9)). For $\text{Cr}(\text{CO})_6$, $\text{Mn}_2(\text{CO})_{10}$, $\text{Co}_2(\text{CO})_8$ and $\text{Co}(\text{CO})_9\text{CH}$ occupations derived from X-ray models agree quite well with those calculated via semiempirical or ab-initio methods.

Many theoretical calculations have been carried out over the last three decades on zero-valent metal carbonyl complexes as well as on cationic and anionic species.

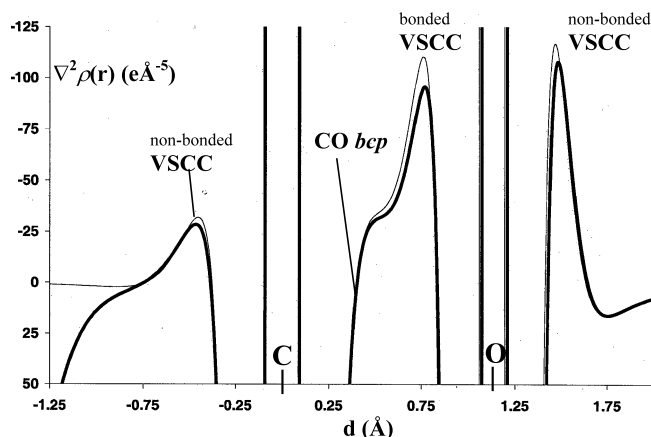


Fig. 2. Profile of the $-\nabla^2\rho(\mathbf{r})$ distribution along the C–O bond path in isolated CO molecule and in $\text{Cr}(\text{CO})_6$ (bold line). The two curves are centred on C. Note the small differences along the C–O bond and at the non-bonded VSCC of the carbon atom. The depletion occurring in the $\text{Cr}(\text{CO})_6$ molecule is due to the interaction with Cr atom. Units as in Fig. 1.

The long-standing discussion about the role of electrostatic and covalent effects in metal–carbonyl bonding has been recently summarised [5b]. A deep analysis of this subject would be beyond the scope of this review and we will focus instead on the electron density properties of the free and complexed carbonyl.

The CO molecule is characterised by a large bond polarity, despite the well known small dipole moment caused by the atomic polarisations of the density, which are opposed to the polarisation of the bond [56]. As a matter of fact, the C–O bcp is shifted towards the least electronegative [40] atom (C) with both valence shells belonging to the oxygen basin. This implies that, at variance from many covalent or polar bonds between atoms of the second row, $\nabla^2\rho(\mathbf{r}_{\text{bcp}}) > 0$. Here, the bcp lies close to a nodal surface of the Laplacian and it is separated from the charge depletion shell of the core density on Carbon. Noteworthy, the three curvatures (λ_i) that sum to give $\nabla^2\rho(\mathbf{r}_{\text{bcp}})$ are larger (in magnitude) than those found for a closed-shell interaction and the two negative ones are almost as large as those for N_2 . A bonded VSCC of C is actually missing because it is overwhelmed by that of oxygen, see Fig. 2. The strong polar character is also revealed by the large $G(\mathbf{r}_b)/\rho(\mathbf{r}_b)$ ratio and atomic charges, while the covalence is manifested by the large $\rho(\mathbf{r}_b)$, $\int_{A \cap B} \rho(\mathbf{r})$ and $\delta(\text{C}, \text{O})$ and the large and negative $H(\mathbf{r}_b)/\rho(\mathbf{r}_b)$ (Table 2). Each atom has one non-bonded VSCC, opposed to the C–O bond. The VSCC on O is associated with a larger $|\nabla^2\rho(\mathbf{r})|$ value, while that on C is more extended in space, see Fig. 3a.

Upon coordination to a neutral transition metal, there are small but not negligible effects on the CO moiety (Table 2). The most important is the C–O elongation

¹⁹ See notes 1–10 in Ref. [55].

Table 2
Properties of the electron density distribution in free CO and in some transition metal carbonyl complexes

Bond A–B	d (Å)	d_{A-bcp} (Å)	d_{B-bcp} (Å)	$\rho(\mathbf{r}_{bcp})$ (e Å ⁻³)	$\nabla^2\rho(\mathbf{r}_{bcp})$ (e Å ⁻⁵)	$H(\mathbf{r}_{bcp})/\rho(\mathbf{r}_{bcp})$ (he ⁻¹)	$G(\mathbf{r}_{bcp})/\rho(\mathbf{r}_{bcp})$ (he ⁻¹)	$\oint_{A\cap B}\rho(\mathbf{r})$ (e Å ⁻¹)	$\delta(A,B)$	$Q(C)$	$Q(O)$
C–O	1.128	0.384	0.744	3.292	15.79	–1.77	2.10	3.17	1.80	+1.16	–1.16
H ₃ BC–O	1.131	0.388	0.743	3.281	12.86	–1.78	2.06	3.17	1.65	+0.87	–1.09
(CO) ₅ CrC–O	1.141	0.389	0.752	3.189	12.42	–1.76	2.03	3.19	1.62	+0.93	–1.11
(CO) ₄ FeC–O _{eq}	1.143	0.390	0.753	3.176	12.15	–1.76	2.02	3.19	1.61	+0.96	–1.12
(CO) ₄ FeC–O _{ax}	1.139	0.389	0.750	3.209	12.56	–1.76	2.04	3.19	1.61	+1.00	–1.11
[(CO) ₃ CoC–O] [–]	1.162	0.395	0.767	3.029	7.95	–1.72	1.90	3.11	1.53	+0.84	–1.20
(CO) ₃ NiC–O	1.137	0.388	0.749	3.217	13.57	–1.76	2.05	3.18	1.66	+1.00	–1.12
[(CO)CuC–O] ⁺	1.117	0.382	0.735	3.385	20.45	–1.79	2.21	3.25	1.82	+1.14	–0.99
										$\delta(M,O)$	$Q(M)$
H ₃ B–CO	1.523	0.495	1.028	0.965	12.65	–0.74	1.66	2.04	0.50	0.04	+1.59
(CO) ₅ Cr–CO	1.928	0.953	0.975	0.716	11.11	–0.28	1.36	2.09	0.83	0.14	+1.13
(CO) ₄ Fe–CO _{eq}	1.822	0.935	0.887	0.941	11.89	–0.38	1.26	2.12	1.05	0.18	+0.72
(CO) ₄ Fe–CO _{ax}	1.829	0.924	0.905	0.881	12.63	–0.35	1.35	2.24	0.98	0.17	
[(CO) ₃ Co–CO] [–]	1.774	0.915	0.859	1.009	13.86	–0.39	1.35	2.14	1.23	0.22	+0.46
(CO) ₃ Ni–CO	1.846	0.932	0.914	0.842	12.43	–0.30	1.34	1.77	0.98	0.16	+0.48
[(CO)Cu–CO] ⁺	1.925	0.945	0.980	0.717	9.20	–0.28	1.18	1.28	0.74	0.09	+0.71

$\oint_{A\cap B}\rho(\mathbf{r})$ is the electron density integrated over the interatomic surface shared by atoms A and B; $\delta(A,B)$ is the delocalisation index between atoms A and B; $Q(A)$ is the atomic charge of atom A, obtained by integrating the electron density over the atomic basin.

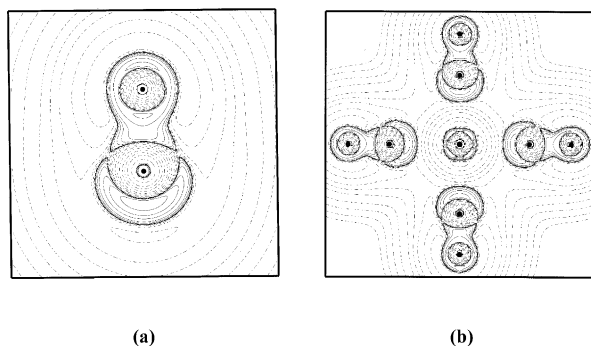


Fig. 3. The Laplacian distribution of the CO molecule in isolated CO (a) and Cr(CO)_6 (b) both at B3LYP/ae level. Contours are drawn with exponential growth, solid lines are negative values.

and the consequent reduction of its associated stretching frequency $\nu_{\text{C-O}}$. All the topological indexes report a weakening of the C–O bonding (smaller $\rho(\mathbf{r}_{\text{bcp}})$, $|H(\mathbf{r}_{\text{bcp}})/\rho(\mathbf{r}_{\text{bcp}})|$, $\oint_{A \cap B} \rho(\mathbf{r})$). As respect to the free CO, the bcp is slightly shifted toward O, and therefore the Laplacian is less positive, because the interatomic surface is less penetrated into the C atomic basin. The non-bonded VSCC on the C atom is slightly decreased by the interaction with the metal. However, the most relevant effects on the Laplacian profile occur along the C–O bond path. The charge of the CO moiety is slightly negative, in virtue of a less positive C atom. Consequently, there is some positive charge accumulation on the metal.

Most of the features of the M–C bond are compatible with its dative (or semipolar) hence ‘intermediate’ character. In fact, an electrostatic interaction is certainly taking place, given the small perturbation of the carbonyl non-bonded VSCC and the location of M–C bcp along the bond path, which is nearly symmetrical only because of the large atomic size of the metal. Indeed, if the non-polar midpoint is considered [41], the shift toward the metal is more clear. However, the orbital contribution cannot be neglected given the relatively large electron density at the bcp (ranging from 0.7 to 0.9 $\text{e } \text{\AA}^{-3}$), the density integrated over the interatomic surface (ca. 2.0 $\text{e } \text{\AA}^{-1}$), the significantly negative $H(\mathbf{r}_{\text{bcp}})/\rho(\mathbf{r}_{\text{bcp}})$ ratio and the number of electron pairs shared ($\delta(\text{M}, \text{C}) \sim 1.0$). The $G(\mathbf{r}_{\text{bcp}})/\rho(\mathbf{r}_{\text{bcp}})$ ratio is always quite large, reflecting the large Pauli repulsion, as predicted by energy breakdown of M–(CO) $_n$ interactions [5b].

Detecting the π -back-donation is difficult, because the cylindrical symmetry of the density along the M–C bond path cleans out traces of preferential accumulation planes. Moreover, charges are sensitive to many different effects (like the polarity of the M–C bond) and therefore cannot be taken as indicators of back-donation. The most reasonable sign of the back-bonding mechanism comes from the $\text{M} \cdots \text{O}$ delocalisation index,

$\delta(\text{M}, \text{O})$. In fact, σ -donation involves mainly the metal and the carbon atoms, while π -back-bonding includes significant $\text{M} \cdots \text{O}$ interaction (see Chart 1). As a matter of fact, for all the transition metal complexes reported in Table 2, $\delta(\text{M}, \text{O})$ is relatively large. In this respect, we can observe the significant differences with the coordination to electron poor atoms of the second row, here exemplified by the H_3BCO complex. The lack of back donation is manifested by the almost unchanged bond length and topological indexes of C–O bonds and by the very small values of $\delta(\text{B}, \text{O})$. Due to the better overlap between two atoms of the same period, the B–C interaction has larger $\rho(\mathbf{r}_{\text{bcp}})$ and $|H(\mathbf{r}_{\text{bcp}})|$ in spite of the smaller electron delocalisation between the two atoms and the almost negligible back-donation.

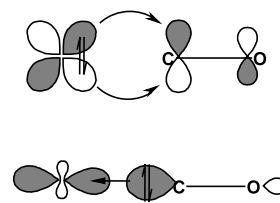


Chart 1.

Changes along a given row of transition metals are less significant and mainly related to the different stereochemistries. Instead, metal carbonyl anions or cations have interesting differences. In $[\text{M(CO)}_n]^{m-}$ systems, the metal–carbon bond is reinforced by the additional back-donation while the C–O bond lengthens, with obvious consequences on the topological indicators. Note in particular the larger $\delta(\text{Co}, \text{O})$ in $[\text{Co(CO)}_4]^-$ and the further shift toward O of C–O bcp, which results in a less positive $\nabla^2\rho(\mathbf{r}_{\text{bcp}})$. On the other hand, in cationic species M–C is weaker and C–O is stronger, as also revealed by the larger experimental $\nu_{\text{C-O}}$. In $[\text{Cu(CO)}_2]^+$, the positive charge is not completely concentrated on the metal and many partitioning schemes address a large $\text{OC} \rightarrow \text{Cu}$ donation and small back-donation [57]. In fact, the computed $\delta(\text{Cu}, \text{O})$ is much smaller than for neutral and anionic transition metal complexes, see Table 2.

As already mentioned, experimental electron density studies in the last decade began reporting details of a topological analysis of the density. Thus, features of theoretical analyses could be compared more easily. Some of the latest studies did in fact concern carbonyl complexes (both mononuclear and polynuclear). Abramov et al. [58] investigated the *cis*- $\text{HMn(CO)}_4\text{PPh}_3$ with an accurate and detailed analysis of the metal–ligand interactions. In particular, they confirmed the features of C–O bond, as previously described. In other works, experimental models failed in correctly predicting the C–O bcp location, exaggerating the shift toward O and

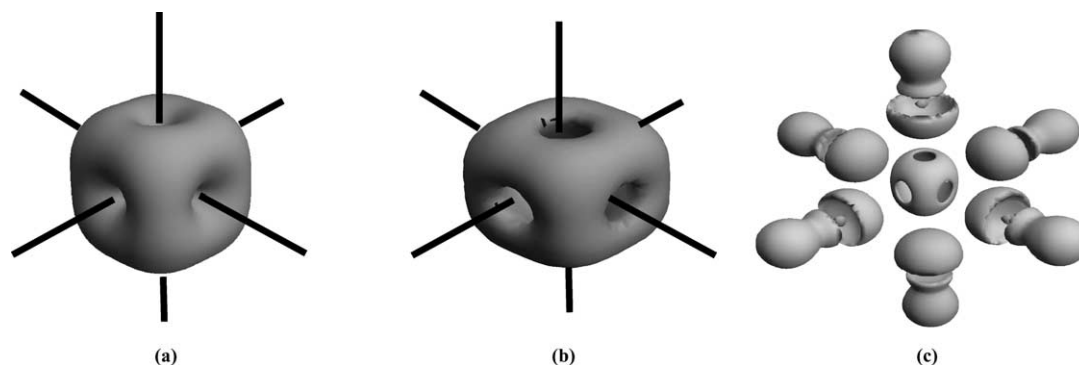


Fig. 4. Features of electron density distribution in $\text{Cr}(\text{CO})_6$: (a) electron density generated by the $\text{Cr}(t_{2g})^6$ configuration (isosurface drawn at $\rho(\mathbf{r}) = 0.6 \text{ e } \text{\AA}^{-3}$); (b) the corresponding Laplacian (isosurface drawn at $\nabla^2\rho(\mathbf{r}) = -2 \text{ e } \text{\AA}^{-5}$, the eight vertexes of the cube surrounding Cr are the i-VSCC's, local maxima of $-\nabla^2\rho(\mathbf{r})$ distribution); (c) Laplacian of the molecular charge distribution calculated at B3LYP/ae level of theory (isosurface $\nabla^2\rho(\mathbf{r}) = -2 \text{ e } \text{\AA}^{-5}$ around the carbonyls and $\nabla^2\rho(\mathbf{r}) = -300 \text{ e } \text{\AA}^{-5}$ around the metal).

resulting in a negative $\nabla^2\rho(\mathbf{r}_{\text{bcp}})$.²⁰ Abramov et al. [58] also described the asphericity of the metal electron density in terms of the Laplacian distribution around Mn. The maxima of $-\nabla^2\rho(\mathbf{r}_{\text{bcp}})$ correspond to the density produced by t_{2g} orbitals in a pseudo octahedral environment and are qualitatively consistent with expectations of LFT. We can focus the prototype $\text{Cr}(\text{CO})_6$ in order to better explain these features. The $(t_{2g})^6$ configuration produces electron density accumulations with a cubic shape around the metal and located at distances of radial maxima of d orbitals (see Fig. 4a). This is highlighted by the Laplacian distribution around the metal. In fact, the vertexes of the cube correspond to eight maxima of $-\nabla^2\rho(\mathbf{r})$ in the 3rd shell, i.e. to eight 'inner-shell' VSCCs (hereinafter i-VSCCs), see Fig. 4b. As a matter of fact, the ligands are found to face regions of low (or even negative) charge concentration occurring on the six faces of the cube.²¹ Therefore, the donor–acceptor interaction can be visually represented as a lump (of the ligand) matching a hole (of the metal), see Fig. 4c. Similar conclusions can be drawn for the other $\text{M}(\text{CO})_n$ complexes, though the polyhedron surrounding the metal centre may change depending on the stereochemistry of the complex; for example, in $\text{Fe}(\text{CO})_5$ it is a trigonal prism.

Gillespie and Bader [59] have studied metals' i-VSCCs, showing the ability of the Laplacian to account for the correct geometries of transition metal molecules. In particular they stressed on the role of the 'ligand-opposed' charge concentrations (in acentric molecules), whose rationalisation led to explain the 'apparent' failures of the VSEPR theory, using the same conceptual arguments.

²⁰ See for example the discussion in Ref. [70]. A similar observation was reported by Bianchi et al. (Ref. [94a]) though stressing on the covalent nature of the C–O bond.

²¹ These depletions spatially correspond to the lobes of the 'empty' e_g orbitals in agreement with LFT prediction.

3.2. Dimeric compounds and the metal–metal bond

Most of the known transition metal dimers and many low nuclearity clusters more or less conform to the 18-valence electron rule when short metal–metal (M–M) contacts are considered as bonds thus offering an indirect evidence for the 'status' of bonds of many M–M interactions. This is particularly cogent in the presence of 'unsupported' M–M contacts when the lack of bridging ligands straightforwardly drives chemists to speak of direct covalent (like in $\text{Mn}_2(\text{CO})_{10}$) or even dative (like in $\text{CrOs}(\text{CO})_{10}$) [60] M–M bonds. However, theoreticians have sometime cast doubts on the nature of these bonds, suggesting that most of the binding energy is actually due to 1,3 $\text{M} \cdots \text{CO}$ interactions [61].

The accurate electron density of a few metal dimers was also studied by X-ray diffraction [62–64]²² but these early studies were made before the QTAM and the multipole model became common practice among crystallographers and, standing on the interpretation of rather noisy deformation density maps, could not produce a clear picture of M–M interactions. Theoretical maps produced very similar results, though, later on, it was recognised that the major weakness of this approach stands principally in the difficult choice of the proper promolecule. In fact, density accumulations in M–M bonds become somewhat visible only by using fragment deformation maps [65,66], i.e. using as promolecule the superposition of computed $[\text{ML}_n]^*$ fragments (rather than spherical atoms).

In the early nineties, QTAM offered a better and less ambiguous theoretical understanding of M–M interactions providing a distinction between unsupported (where a M–M bond path is found) and ligand bridged (where a M–M bond path is not found) species [67,68].

²² In Ref. [64] the multipolar model was adopted, thus model deformation density maps could be produced.

More recently QTAM was used for the interpretation of the experimental charge density of $\text{Mn}_2(\text{CO})_{10}$ [69] and $\text{Co}_2(\text{CO})_6(\text{AsPh}_3)_2$ [70] confirming the presence of a (3,−1) critical point between the two metal atoms. However, while we considered the Co–Co interaction as a genuine covalent bond [70], Bianchi and co-workers defined the Mn–Mn interaction as ‘closed-shell’ and classified the Mn–Mn bond as metallic with features ‘between ionic and covalent’ [69b]. The main argument was the positive Laplacian found at the M–M bcp. Based on a similar reasoning, Uhl et al. [71] classified as closed shell the Ni–Ni interaction in $\text{CpNi}(\mu\text{-InCH}_3)_2\text{NiCp}$.

Closed shell or open shell refer to the electronic configuration of the isolated fragments, that eventually produce a chemical bond but, once the molecule is formed, such rigorous attribution is no longer possible. Moreover, the electron density itself cannot give this information, unless resorting to the phenomenological correspondence with prototype situations, assumed on the basis of common chemical sense. As mentioned above, it was shown by Bader that a simple ‘translation’ of the orbital concepts using the Laplacian distribution is possible for second and third row molecules (see Table 1) [6], but it becomes more difficult if heavier atoms are concerned [48,72], due to the absence of VSCC in some elements of the fourth and following rows. The concept of ‘shared interaction’ is often associated with the presence of charge concentration in the interatomic region. However, it mainly implies the concerted movement of a certain fraction of electrons in two (or more) atomic basins. It is true that covalent bonds between first (es H–H) and second row (es $\text{H}_3\text{C}-\text{CH}_3$) atoms are associated with large charge concentrations along the bond path, resulting from the considerable orbital overlap. This nicely correlates with the estimated dissociation energies, at least as far as orbital energies only are concerned. On the other hand, equivalent bonds of the third and fourth row atoms are characterised by smaller charge concentrations (or even charge depletions) and they are associated with smaller dissociation energies. Within the QTAM approach, the correct indicator for the electron-sharing concept is the delocalisation index δ , whose definition is in fact based on the presence of the same electron pair(s) in two atomic basins. On the other hand, δ is unable to address the strength of a chemical bond, which is better described by the amount of $\rho(\mathbf{r})$, $\oint_{A \cap B} \rho(\mathbf{r})$, $H(\mathbf{r})$ and $\nabla^2 \rho(\mathbf{r})$ for covalent bonds, or by the atomic charges for ionic bonds. It should be recollected that a covalent bond of a given order (say $n=1$) may be indefinitely strong or weak, based only on the atomic types involved, their oxidation states and their chemical environments (hybridisation). For example, Na–Na is much weaker than its homologous H–H (the dissociation energies are ca. 15 vs. 100 kcal mol^{−1}). In fact, they have a similar

electronic mechanism for the bonding, [73] but Na–Na has a much lower orbital overlap (caused by the more diffuse valence electrons) and therefore a smaller electron density in the bonding region. Nevertheless, it remains well above a pure neutral closed-shell interaction such as that between two noble gases (< 0.5 kcal mol^{−1}). Simplifying the results of Berlin’s partitioning, we easily understand that covalent bonding produced by diffuse electrons results in small stabilisation energy. In this context, saying that an homopolar metal–metal bond has ‘intermediate features between covalent and ionic’ [69b] is extremely misleading for understanding the actual bonding mechanism. Neither we can recognise a metallic behaviour in isolated dimeric molecules.

In our opinion, more appropriate knowledge could be extracted by a QTAM analysis of the densities in the realm of metal clusters, provided that some typical features of transition metals are taken into account: (a) the co-presence of contracted $(n-1)d$ and diffuse ns electrons in the valence shell; (b) the absence of charge concentration in the outermost shell of all transition metals; (c) the large total number of core electrons; and (d) the large atomic sizes (features which all leave recognisable traces in the Laplacian distribution, either at atomic level and in the molecule). To exemplify our approach we will here discuss the main results of our topological analysis of the experimental electron density in $\text{Co}_2(\text{CO})_6(\text{AsPh}_3)_2$, ‘iso-electronic’ with $\text{Mn}_2(\text{CO})_{10}$, though characterised by the presence of two kinds of interaction between heavy elements (namely the ‘covalent’ Co–Co and the ‘dative’ As–Co bonds), which are summarised in Fig. 5 [70]. The most relevant feature is of course the presence of a metal–metal bond path and the absence of 1,3 M··CO interactions. In the original paper, it was suggested that possible evidence of some CO contribution may come from the shape of the Co–C bond paths which are slightly bent toward the opposite Co,²³ perhaps due to some overlap between carbonyls π or π^* and metal d_{z^2} orbitals. The Laplacian of the equatorial carbonyls is also slightly perturbed toward the vicinal Co. This can be better confirmed by theoretical investigation of the delocalisation index and bond order. Calculations on the D_{3d} conformation of $\text{Co}_2(\text{CO})_8$ (thus, without bridging carbonyls, see Fig. 6a) show that $\delta(\text{Co},\text{Co})$ is not 1.0 as it occurs for Na_2 or K_2 . On the contrary, the delocalisation between the two metals is only partial (ca. 0.5). Interestingly, the ‘residual electrons’ are shared between the metals and all the vicinal carbonyls. It is a small contribution, but it occurs for six 1,3 Co–C interactions and it is eventually significant. In this way, we can recover the whole electron pair associated with a single M–M interaction

²³ In fact the two Co–Co–C geometrical angles are 86.8° and 85.4°, while the bond path angles are 86.1 and 84.7°, respectively (Ref. [70]).

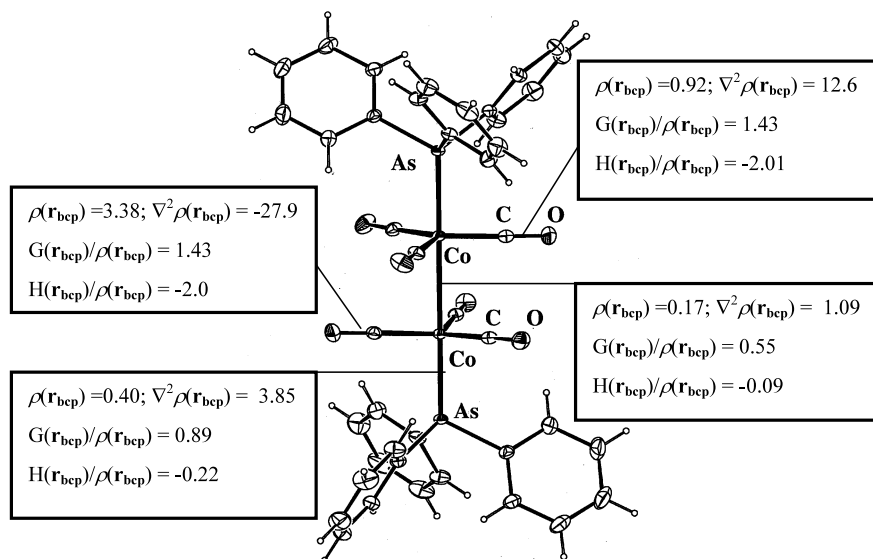


Fig. 5. An ORTEP plot of $\text{Co}_2(\text{CO})_6(\text{AsPh}_3)_2$ with topological parameters determined from the experiment [70]. Units are as in Table 1. The molecule lies on a crystallographic threefold axis and it has a pseudo inversion centre. The parameters of Co–As, Co–C and C–O are averaged between two independent bonds. In addition, these numbers are slightly different from those in the original publication, due to some correction applied to the xD code [23]⁴.

by summing up the direct $\delta(\text{Co}–\text{Co})$ and the six $\delta(1,3\text{Co}–\text{C})$ (Fig. 6a). It is notable that while the 1,3 interactions are here unable to give rise to a bond path, they have anyway a significant role in the bonding, as we will see in detail when speaking of bridged and semibridged systems (see Section 3.3).

Other features of the M–M interaction are important and deserve attention (Fig. 6a). First, while the electron density at the bcp is small (about $0.2 \text{ e } \text{\AA}^{-3}$), $\rho(r)$

integrated over the interatomic surface is actually large (ca. $1.5 \text{ e } \text{\AA}^{-1}$) and close to the typical values of many single bonds of p-block atoms of second rows (see Table 1). This confirms the diffuse character of the electrons involved in the bonding, which is responsible of the small $\rho(r_{\text{bcp}})$ and the positive (or slightly negative) $\nabla^2\rho(r_{\text{bcp}})$. The energy densities computed at the M–M bcp are also quite indicative. In fact, at variance from well established closed-shell interactions, $H(r_{\text{bcp}})$ is

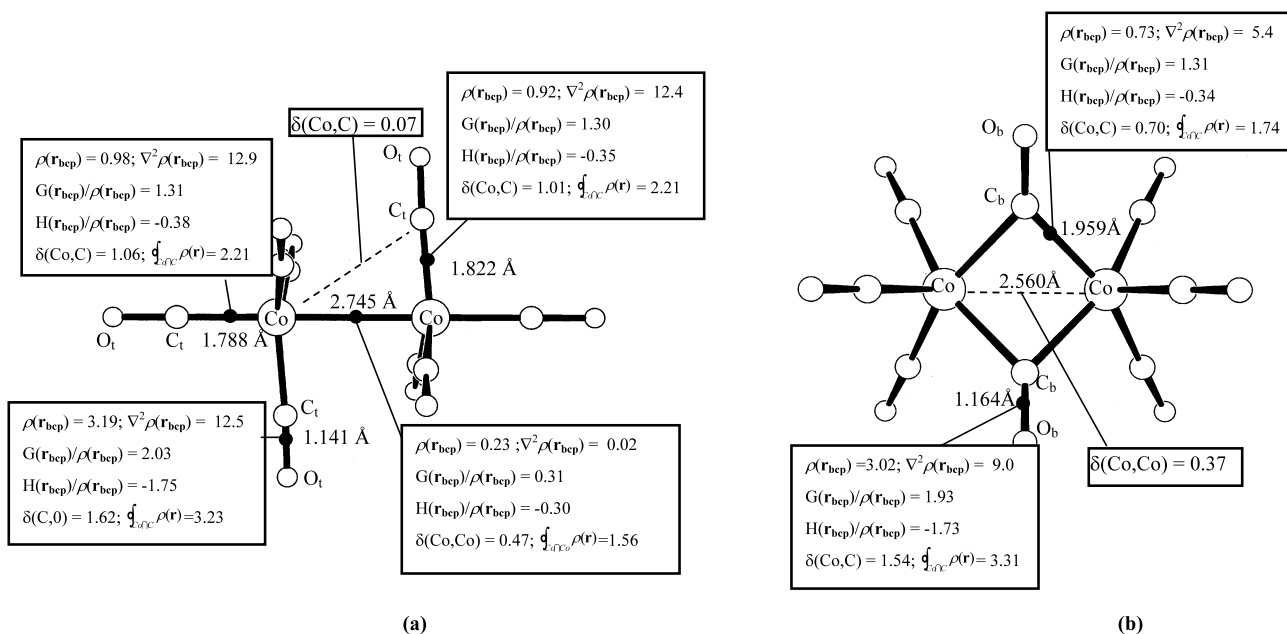


Fig. 6. D_{3d} (a) and C_{2v} (b) isomers of $\text{Co}_2(\text{CO})_8$ with topological indexes of principal interactions. Units are as in Table 1. Solid lines indicate the presence of corresponding bond paths, while dashed lines are traced between atoms not directly linked, though characterised by significant delocalisation indexes.

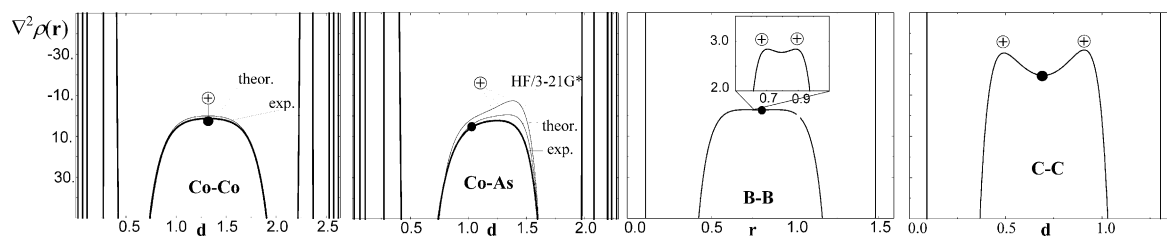


Fig. 7. Profile of the Laplacian distribution for Co–Co, Co–As bonds (in $\text{Co}_2(\text{CO})_6(\text{AsPh}_3)_2$), B–B in $\text{B}_2(\Sigma_g^3)$ and C–C in a phenyl ring, (from experimental analysis and HF/ae calculation) [70]. The position of the bcp's (filled dot) and of $-\nabla^2\rho(\mathbf{r})$ maxima (+) are reported. The B–B interaction is quite representative of covalent bonds between atoms with rather diffuse valence density, thus producing small charge concentration at the bcp (compared to C–C, for example). The missing valence shell in atomic Co makes the Co–Co bond lacking of a pure charge concentration. Units as in Fig. 1.

negative (albeit small) speaking for a dominant potential energy density. Compared to $H(\mathbf{r}_{\text{bcp}})/\rho(\mathbf{r}_{\text{bcp}})$ ratios typical of single bonds between second row atoms, M–M interactions reveal a weaker covalency in agreement with the calculated dissociation energies. The kinetic energy density at the M–M bcp is close to the expected values for homopolar covalent bonds ($G(\mathbf{r}_{\text{bcp}})/\rho(\mathbf{r}_{\text{bcp}}) \leq 0.5 \text{ he}^{-1}$) and different from neutral closed-shell interactions ($G(\mathbf{r}_{\text{bcp}})/\rho(\mathbf{r}_{\text{bcp}}) \geq 1 \text{ he}^{-1}$).

Finally, the shape of the Laplacian profile along the Co–Co bond path closely resembles that of B–B bond in $\text{B}_2(\Sigma_g^3)$, an undisputed covalent bond between atoms that have a valence shell quite diffuse compared to C atoms (Fig. 7). In fact, it is the diffuse character of 4s electrons involved in M–M interactions that hamper the formation of a considerable charge concentration in the bonding region. The same occurs for covalent dimers of the second and third row metals or semimetals whose charge concentration along the bonding, if any, is extremely poor (Table 1).

An interesting analysis was reported by Jansen et al. [74], who characterised theoretically hetero-bimetallic systems containing Co–Ti and Co–Zr unsupported bonds. Many features of the electron density are similar to those of Co–Co or Mn–Mn bonds described above, but for the more positive charge on Ti or Zr and the asymmetrical location of the interatomic surface. A classification of these bonds based only on the analysis of electron density distribution was problematic. By adding information from the electron localisation function [75], the authors could reveal a weak covalency (an electron localisation domain for the M–M bond is always found) and a high polarity (the domain lies in the atomic basin of Co and it has a low localisation).

3.3. Carbonyl bridged and semibridged systems

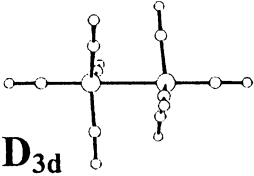
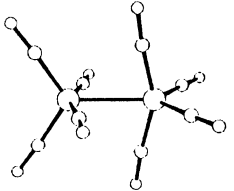
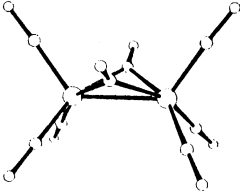
As we outlined in the previous section, unsupported homonuclear and heteronuclear dimers have been widely investigated with theoretical methods for the inductively supposed direct metal–metal interaction. On the other hand, μ -CO bridged systems provide complementary information, due to the induced stereochemical

rearrangement of the M–M moiety. Many supported interactions have been studied with either experimental and theoretical analysis of the electron density distribution. Here, we will focus in particular on CO bridged systems. There are two well-known first transition homoleptic dimers containing carbonyl bridges and a single M–M bond (within the 18-electron rule formalism): $\text{Fe}_2(\text{CO})_9$ and $\text{Co}_2(\text{CO})_8$. Both received enormous attention from theoreticians, though the former could not be studied with accurate crystallographic techniques, because of severe problems in re-crystallising the species [76].²⁴

The gas phase potential energy surface of $\text{Co}_2(\text{CO})_8$ is characterised by three minima [77,78] (see Table 3), representative of terminal, semibridging and bridging coordinations (I, II and III in Fig. 8). Their relative stability is severely model-dependent (in agreement with Schaefer [77]) and the energy window is quite small, giving an easy explanation for the observed fluxionality. However, only the C_{2v} (doubly bridged) structure has been observed in the solid state. Leung and Coppens [64] re-determined the X-ray crystal structure of $\text{Co}_2(\text{CO})_8$ and analysed the deformation density of the molecule. The geometry resembles that of $\text{Fe}_2(\text{CO})_9$ because the 'missing' bridging carbonyl does not lead to an extensive geometrical reorganisation and it just leaves an 'empty' site. The Co–Co distance is shorter than that of the unsupported isomer and the bridging carbonyls have longer Co–C_b and C_b–O_b distances. The lack of residuals in the M–M region and the shape of 5σ density around the bridging carbonyls led the authors to speak of a through bond interaction [64], in agreement with an earlier theoretical study [66]. Low et al. [65a] examined theoretical deformation density of $\text{Co}_2(\text{CO})_8$, addressing some differences from the experimental results, which were ascribed to thermal smearing. In particular, some Co–Co bent bonding density accumulation was found, though justified as a 'constructive

²⁴ The crystal structure, published by Cotton and Troup was determined by the lucky finding of a single crystal directly from a large commercial sample.

Table 3
Collection of pertinent parameters of the equilibrium $[M_2(CO)_8]^{q-}$ isomers optimised at B3LYP/ecp level

Molecular Structure	Compound	Energy kcal/mol	d_{M-M} Å	$d_{(M-C)opp.}$ Å	$d_{(M-C)prox.}$ Å	$d_{M...Cprox.}$ Å	$d_{(C-O)opp.}$ Å	$d_{(C-O)prox}$ Å	M-C-O _{prox} °	Imag. Freq.
 D_{3d}	$Co_2(CO)_8$	3.6	2.69	1.78	1.81	3.11*	1.147	1.150	177.6	0
	$[FeCo(CO)_8]^-$	3.0	2.82	1.74; 1.76	1.79; 1.78	3.07*; 3.28*	1.164; 1.160	1.159; 1.164	177.5; 175.5	0
	$[Fe_2(CO)_8]^{2-}$	0.0	2.89	1.73	1.77	3.22*	1.179	1.175	175.4	0
 D_{2d}	$Co_2(CO)_8$	0.0	2.64	1.80	1.79	2.85*	1.148	1.151	175.1	0
	$[FeCo(CO)_8]^-$	0.0	2.68*	1.76; 1.76	1.79; 1.81	2.29; 3.01*	1.162; 1.163	1.159; 1.176	178.8; 153.1	0
	$[Fe_2(CO)_8]^{2-}$	1.2	2.78	1.74	1.78	2.92*	1.180	1.174	174.0	0
 C_{2v}	$Co_2(CO)_8$	3.1	2.55*	1.81	1.95	1.95	1.146	1.171	139.2	0
	$[FeCo(CO)_8]^-$	4.0	2.59*	1.78; 1.78	1.90; 2.07	2.07; 1.90	1.161; 1.160	1.181	147.2; 131.4	1
	$[Fe_2(CO)_8]^{2-}$	5.9	2.64*	1.73	1.98	1.98	1.179	1.195	138.2	1

For each stereochemistry, we distinguish ‘opposed carbonyls’ (having $M-M-C > 90^\circ$) and ‘proximal carbonyls’ (having $M-M-C < 90^\circ$). For each compound the energy is related to the most stable isomer. In $[FeCo(CO)_8]^-$, the first entry refers to Fe–CO parameters, the second to Co–CO. A bond path characterises all the interactions but those labelled with *.

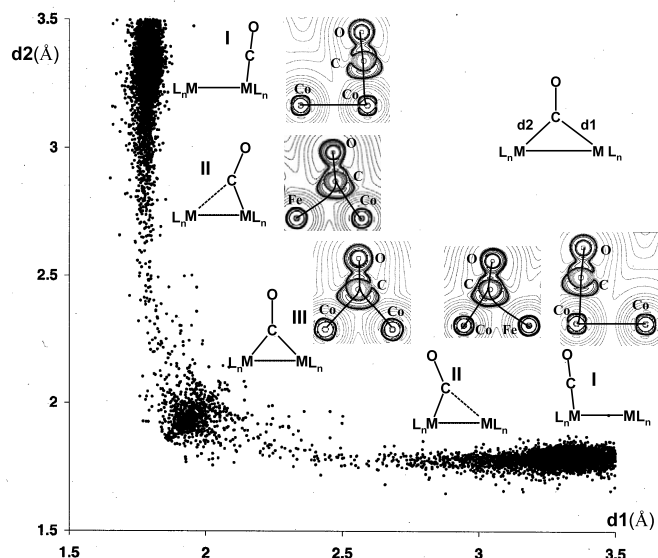


Fig. 8. A symmetrised correlation plot for the moiety $M(CO)M$; each point represents a fragment retrieved from the CSDS [87]. $\nabla^2\rho(r)$ in planes containing unsupported, semibridged and symmetrically bridged $M-M$ interactions are from accurate electron density determination in $Co_2(CO)_6(AsPPh_3)_2$ [70], $[FeCo(CO)_8][PPN]$ [91] and $Co_4(CO)_{11}PPh_3$ [85]. Note that pictures have different features around the Co atoms than those in the original publication, due to some correction applied to the XD code [23]⁴.

interference', because a topological analysis of the total density did not reveal any direct Co–Co bond path. In fact, in terms of QTAM the most relevant difference between bridged and unbridged isomers is the absence or presence of a $M-M$ bond path. This was first reported by MacDougall [67a], using minimal basis set and HF level of theory, and subsequently confirmed using more extensive bases [65a]. We can also support the correctness of the original analysis by studying the optimised geometry at DFT level of theory with ae and ecp basis sets, see Fig. 6b.

A long theoretical debate accompanied $Fe_2(CO)_9$. While empirical rules would predict a direct Fe–Fe bonding, many MO calculations (semi-empirical or ab initio) concluded that no interaction is actually taking place between the two metals given the small d overlap [79], though VB calculations provided more evidence for it [80]. According to an extended Hückel fragment MO analysis, Mealli and Proserpio [81] concluded that a Fe–Fe bond is formally present even if the through-bond intermetal repulsion does overcome the attractive through-space Fe–Fe interaction. A QTAM analysis was reported by MacDougall [67a] and by Bo et al. [68], who did not find a direct $M-M$ bond path and concluded that ' $Fe_2(CO)_9$ is build up by the bridging carbonyls' [68], in agreement with the earlier suggestion by Summerville and Hoffmann [82]. Bo et al. also noted many features of the μ_2 -coordination (that we confirm by more accurate calculations): the larger envelope of the valence shell surrounding the carbon, indicative of a more delocalised bonding through the metals; a larger electronic population on the carbonyl carbon, as a

consequence of the better metal-to-ligand charge transfer in the bi-coordinative mode; the presence of two non-bonded VSCCs on the bridging oxygen, speaking for an incipient re-hybridisation, though associated with a smaller basicity compared to organic ketones (given the values of $\nabla^2\rho(r)$ at the VSCCs). In addition, the bond delocalisation was confirmed by the analysis of the Fermi hole density maps [68].

Additional features of $M_2(\mu-CO)$ bridged systems are noteworthy. The $M-C_b$ bond paths have a concave curvature inside the MC_bM cycle, suggesting that the carbon sp hybridisation is overwhelming the sp^2 one, though the enlarged Laplacian envelope confirms that some mixing is actually occurring. In many ring systems, inward curvatures of the paths are representative of bond delocalisation, while outward curvatures are related to localisation of a strained bond [83]. The delocalisation indexes do in fact confirm this hypothesis, as the $\delta(M-M)$ is still quite significant (about 0.35) despite the lack of a direct metal–metal path. Moreover, $\delta(C_b-C_b)$ is also quite relevant, suggesting a strong delocalisation throughout the four-atom butterfly cycle in $Co_2(CO)_8$ and the five-atom bipyramidal cage in $Fe_2(CO)_9$.²⁵ The $M-C_b$ bonds are characterised by relatively large electron density, speaking for a bond order greater than simply one half $M-C_t$, as also supported by $\delta(M-C_b)$. Very interestingly, $\delta(M-O_b) \sim \delta(M-O_t)$ suggests that π -backdonation from

²⁵ Of course a rcp and a ccp in the middle of the $M-M$ region characterise the molecular graph of $Co_2(CO)_8$ and $Fe_2(CO)_9$, respectively.

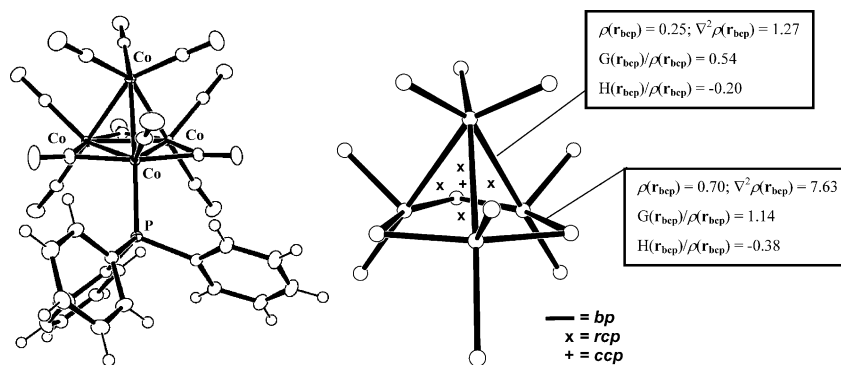


Fig. 9. Left: ORTEP view of the cage $\text{Co}_4(\text{CO})_{11}(\text{PPh}_3)$, from the experimental determination [85]. Right: schematic representation of the electron density topology in the cage and symmetry averaged topological indexes of Co_{basal}–Co_{apical} and Co–C_b bonds (units are as in Table 1). Numbers are slightly different from those in the original publication, due to some correction applied to the XD code [23]⁴.

each metal is almost constant despite the larger M–C_b separations. Thus, the overall electron flow received by a bridging carbonyl is about two times that received by a terminal CO. This would agree with both the structural parameters of C_b–O_b (larger distance, smaller stretching frequency) and with the computed atomic charges that report bridging carbonyls more negative than terminal. Indeed, experimental works presently underway in our laboratory confirm the greater affinity of bridging carbonyls toward cationic species, in agreement also with computed and experimentally derived electrostatic potentials [84].

The first experimental validation of the electron density distribution in μ -CO systems came from the analysis of the tetrahedral cluster $\text{Co}_4(\text{CO})_{11}(\text{PPh}_3)$ [85], see Fig. 9. In agreement with HF/ae calculations on the C_{3v} $\text{Co}_4(\text{CO})_{12}$ isomer [86],²⁶ no direct Co–Co bond paths were found for the three bridged edges (whose overall topological features resembled those previously described for $\text{Co}_2(\text{CO})_8$). In contrast, the unsupported Co–Co interactions are associated with bp's, with topological features close to those previously observed for $\text{Co}_2(\text{CO})_6(\text{AsPh}_3)_2$.

Analysing the geometries of dimeric and polynuclear species present in the Cambridge Structural Database (CSD) [87], no substantial discontinuity between terminal (I) and symmetrical bridging (III) coordination modes is observed (see Fig. 8) [88]. Conformations I and III are reasonably well defined but a clear breakdown between the three bonding modes is not possible. The conformation II is associated with the central region, tentatively confined in the 2.0–3.0 Å M...C distance range. In Table 3, we report features of the potential energy surface exploration for some $[\text{M}_2(\text{CO})_8]^{q-}$ species. At variance from $\text{Co}_2(\text{CO})_8$, $[\text{FeCo}(\text{CO})_8]^-$ and $[\text{Fe}_2(\text{CO})_8]^{2-}$ have only two true minima, of symmetry

D_{2d} and D_{3d} (in $[\text{FeCo}(\text{CO})_8]^-$, C_s and C_{3v}). In the solid state, the former is known for $[\text{FeCo}(\text{CO})_8]^-$ [89], the latter for $[\text{Fe}_2(\text{CO})_8]^{2-}$ [90].²⁷ As we learn from theoretical calculations reported in Table 3, the molecular graph corresponding to coordination mode I is always characterised by a M–M bond path, which is instead invariably missing in symmetric bridging coordination III.²⁸ On the other hand, the semibridging mode II has a topology similar to I in $\text{Co}_2(\text{CO})_8$ and $[\text{Fe}_2(\text{CO})_8]^{2-}$ and similar to III in $[\text{FeCo}(\text{CO})_8]^-$, where in fact the semibridging character is more pronounced. The topology of the latter complex has been recently confirmed experimentally [91].

According to the structure correlation method, Fig. 8 is a representation of the terminal-to-bridging CO reaction path, i.e. a track of the elementary mechanism associated with most fluxional processes of carbonyl metal clusters. It is interesting to describe such elementary process by considering the evolution of the electron density and its derived quantities along the terminal-to-bridging CO coordinate (here simplified by the variation of M–M–C angle). While it is theoretically possible following the 'same' molecule along a given conformational rearrangement, the structure correlation principle resorts to the concept of fragment in order to observe the 'same' moiety in different environments, each 'photographed' at its equilibrium geometry. Accordingly, we can compare the calculated evolution of the electron density along the terminal-to-bridging CO path to the picture emerging from a correlation-like plot (Fig. 8) of three experimental results on $[\text{Co}_2(\text{CO})_6(\text{AsPh}_3)_2]$

²⁷ See also Ref. [89]. Recently, the C_{2v} isomer (which is not a minimum in the gas phase) has been observed in the strong polarising environment produced by Li cations [90e].

²⁸ In $[\text{Fe}_2(\text{CO})_8]^{2-}$ and $[\text{FeCo}(\text{CO})_8]^-$ the coordination III is not associated with a stable isomer, since the corresponding equilibrium geometries have at least one imaginary frequency. However, the theoretical observation that symmetric bridges quench the M–M bond path is well supported in many analogous fragments.

²⁶ The crystal structure of $\text{Co}_4(\text{CO})_{12}$ is affected by a severe dynamical disorder and therefore is unsuitable for an accurate electron density study.

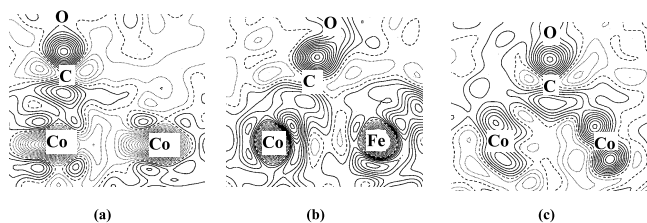


Fig. 10. The experimental deformation density in planes containing unsupported (a), semibridged (b) and symmetrically bridged (c) M–M interactions, from accurate electron density determination in $\text{Co}_2(\text{CO})_6(\text{AsPPh}_3)_2$ [70], $[\text{FeCo}(\text{CO})_8][\text{PPN}]$ [91] and $\text{Co}_4(\text{CO})_{11}\text{PPh}_3$ [85], respectively. Contours are drawn at $\pm 0.05 \text{ e } \text{\AA}^{-3}$. Solid contours are positive values, dotted contours are negative; the dashed line corresponds to $\Delta\rho(\mathbf{r}) = 0.0$.

[70], $[\text{FeCo}(\text{CO})_8][\text{N}(\text{PPh}_3)_2]$ [91] and $[\text{Co}_4(\text{CO})_{11}(\text{PPh}_3)]$ [85], which are representative of conformation I, II and III, respectively. The metamorphosis from a terminal to a bridging carbonyl has been theoretically examined on $[\text{FeCo}(\text{CO})_8]^-$ [91], by exploring the neighbourhood of the actual C_s minimum on the potential energy surface.

The main changes observed in the theoretical electron density distribution upon bending of the Co–C bond to form a bridging arrangement (Co–C–Fe) are summarised in the following points.

3.3.1. Deformation density

As we mentioned above, the deformation density in the intermetal region is always featureless. As Fe–Co–C angle (θ) decreases, a small accumulation along the $\text{Fe} \cdots \text{C}$ direction is observed, see Fig. 10 for the experimental deformation densities. In $[\text{FeCo}(\text{CO})_8]^-$, it is quite notable that most of the ‘donor’ density surrounding the semibridging carbon is still directed toward the cobalt atom, though it is no longer associated with a ‘hole’ in the metal 3d shell density, as typically occurs for terminal carbonyls. Eventually, symmetric bridging conformation reveals an enlarged donor density, again without peaks between the two metals.

3.3.2. Molecular graph

For a fully terminal system the molecular graph is characterised by the Co–Fe and the Co–C bond path, without any $\text{Fe} \cdots \text{C}$ direct interaction. As we noted above, the bp linking the metal to a terminal carbonyl in equatorial position is slightly bent in the direction of the proximal metal (see the bond path angles $\alpha 1$ and β in

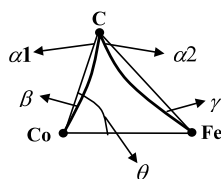


Chart 2.

Chart 2 and Fig. 11). A Fe–C bond path appears for $\theta < 70^\circ$, where the molecular graph is characterised by a ring. The rcp, initially very close to the Fe–C bp, moves toward the Co–Fe bp with whom it eventually coalesces and disappears for $\theta < 65^\circ$. This corresponds to a catastrophe point (where the molecular graph undergoes abrupt changes) of the bifurcation type, i.e. characterised by the presence of degenerate critical points (rcp–bcp) in the electron density distribution [6]. The lack of the Co–Fe bond path persists on further bending of the carbonyl toward Fe.

The Fe–C bond path is extremely inwardly curved in the initial steps (see the bond path angle $\alpha 2$ in Fig. 12) but this curvature decreases as the Fe–C bond reinforces. It is also quite interesting following the evolution of bond path angles at the metals (β and γ in Fig. 12), both having an inward curvature.

We can summarise the observations as follows:

- angles at carbon ($\alpha 1$, $\alpha 2$) measure the relative C \rightarrow M donation, the larger is the deviation from a straight path, the weaker is the contribution; thus, since $\alpha 1 < \alpha 2$ the donation to Co is larger than that to Fe until the system reaches a symmetrical arrangement (and $\alpha 1 \sim \alpha 2$).
- angles at the metals (β , γ) reflect the M \rightarrow C back-donation; since γ is always small, back-donation must be quite significant even for incipient semibridging coordination.
- Assuming that distortions of the valence shell distribution equally affect the metals and the carbon, from $\beta + \gamma < \alpha 1 + \alpha 2$, we may tentatively conclude that (Co,Fe) \rightarrow C back-donation overwhelms C \rightarrow (Co,Fe) donation along the conversion and it is definitely more important in the symmetric bridging mode II.

3.3.3. Laplacian distribution

The envelope of negative Laplacian of $\rho(\mathbf{r})$ surrounding a terminal carbonyl carbon is similar to that of an uncoordinated CO, though slightly distorted toward the proximal metal. The distortion increases as the carbonyl bends and the envelop becomes definitely larger in the symmetric bridge conformation, preserving however a unique maximum (i.e. a VSCC), see Figs. 8 and 11. The single non-bonded VSCC of the oxygen is initially opposed to the proximal metal, though along the conversion coordinate it moves on the other side (i.e. toward the proximal metal). After the ring graph is broken, a second non-bonded VSCC appears and the two C–O–VSCC angles approach 130° , see Fig. 13. The i-VSCCs of the metals (i.e. those of the 3d shell) also undergo a substantial modification. In unsupported conformations, they typically generate a polyhedron whose faces are occupied by CO ligands or by the M–M bond, see Fig. 13. The conformational rearrangement

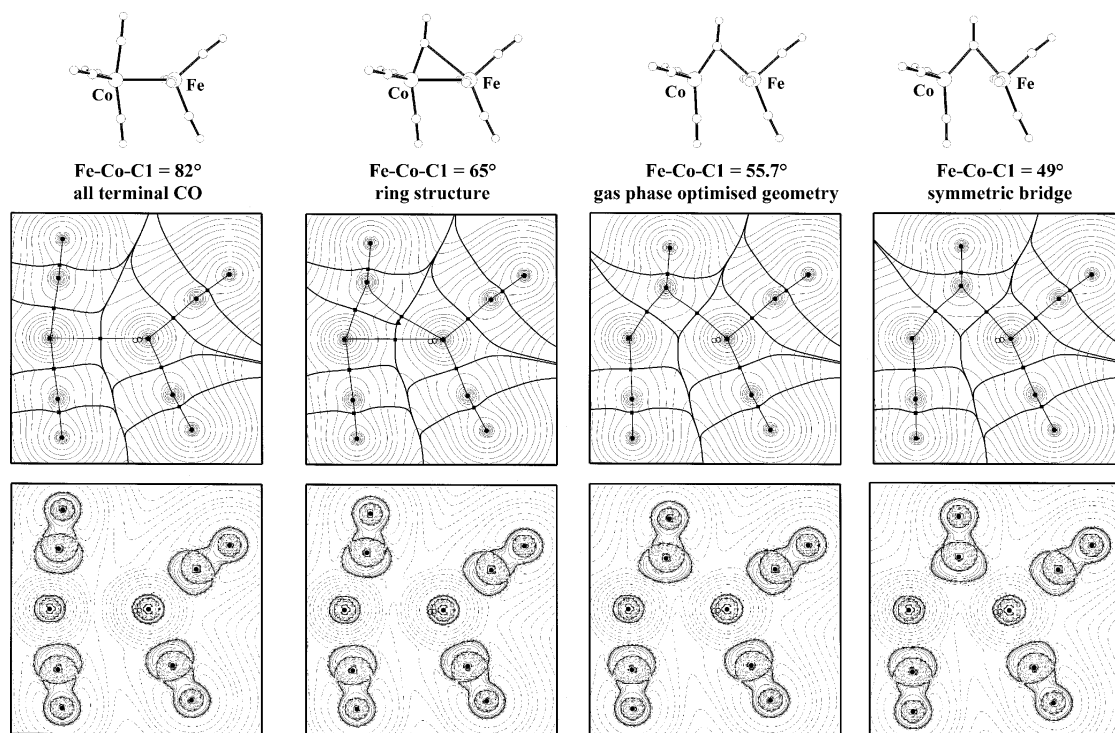


Fig. 11. Geometries, total electron density distribution (with molecular graphs superimposed) and Laplacian of four points along the terminal to bridging conversion path calculated for $[\text{FeCo}(\text{CO})_8]^-$, at B3LYP/ae level [91]. For sake of simplicity, the geometry of the molecule was fixed on the gas-phase optimisation but for the 'bridging' carbonyl.

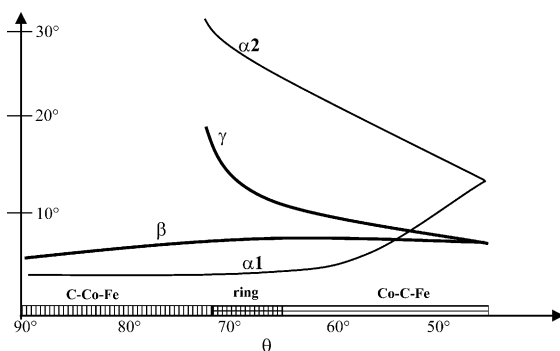


Fig. 12. Idealised evolution of bond path angles (as defined in Chart 2) along the CO bending in $[\text{FeCo}(\text{CO})_8]^-$ (from Ref. [91]).

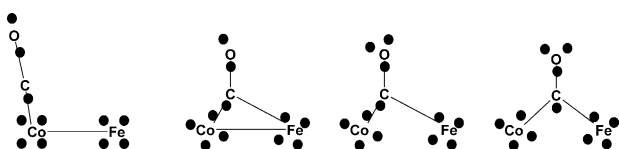


Fig. 13. Scheme with positions of metal i-VSCC's and carbonyl VSCC's along the CO bending. The disposition of metal's i-VSCC's is here idealised with a square, though their actual shape depends on the stereochemistry of metal coordination.

occurring upon bending induces also a rotation of the i-VSCC polyhedra surrounding the two metals. It is notable that the conformation adopted in the semibrid-

ging and bridging modes seems to favour the back-donation mechanism.

3.3.4. Atomic charges

The QTAM charge accumulated on a carbonyl increases upon its bending. In neutral species: $Q(\text{CO}_t) \approx -0.2$ and $Q(\text{CO}_{sb}) \approx Q(\text{CO}_b) \approx -0.4$. In $[\text{FeCo}(\text{CO})_8]^-$ before the carbonyl bending the negative charge is mostly localised in the $\text{Fe}(\text{CO})_4$ moiety ($Q \sim -0.6$). At the equilibrium geometry the two parts of the molecule have an almost identical charge and eventually $Q[\text{Fe}(\text{CO})_4] \sim -0.15$ in the symmetric bridge conformation. The charge equalisation occurring in the semibridging conformation is confirmed by the experimental monopoles and it is in agreement with the metal–carbonyl bond distances observed, which speak for an intermediate charge on both fragments²⁹ (Table 3).

3.3.5. Bond indexes

The main changes occurring can be summarised as follows:

- $\rho(\mathbf{r}_b)_{\text{Co-Fe}}$ is quite constant until the associated bond path breaks; when the M–M–C ring is

²⁹ In fact, both Co–C and Fe–C terminal carbonyl distances are intermediate between those optimised in neutral and mono-anionic complexes.

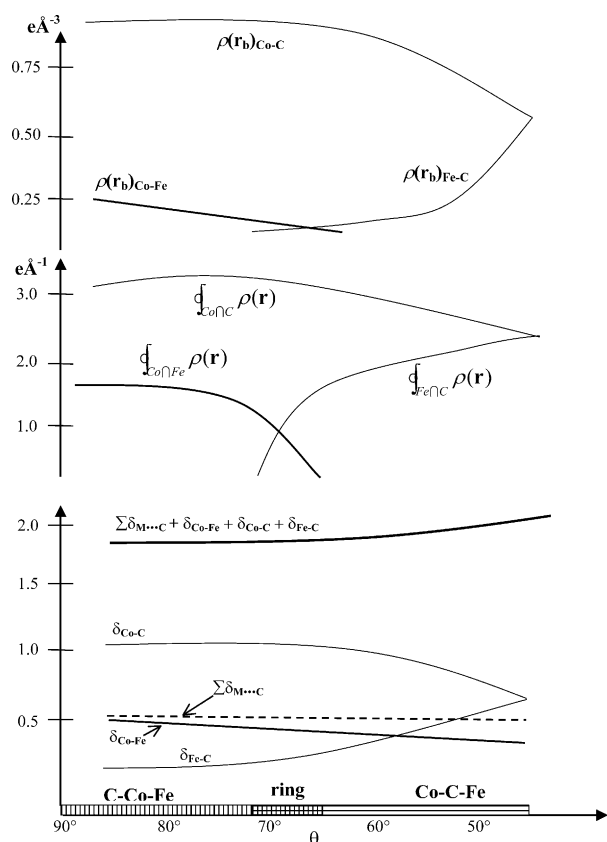


Fig. 14. Idealised evolution of topological indexes $\rho(r_{bcp})$, $\int_{A \cap B} \rho(r)$ and $\delta(A,B)$ along the CO bending in $[\text{FeCo}(\text{CO})_8]^-$ (from Ref. [91]).

formed, $\rho(r_b)_{\text{Fe}-\text{C}} < \rho(r_b)_{\text{Co}-\text{Fe}}$, but it rapidly increases up to the value of a symmetric bridging coordination, where $\rho(r_b)_{\text{Fe}-\text{C}} = \rho(r_b)_{\text{Co}-\text{C}}$, see Fig. 14.

- b) The three corresponding $\int_{A \cap B} \rho(r)$ show similar evolutions, though with a more pronounced decrease of Co–Fe density, see Fig. 14.
- c) $\delta(\text{Co}-\text{Fe})$ smoothly decays, while $\delta(\text{Fe}-\text{C})$ grows more rapidly; all the other metal–proximal carbonyl delocalisation indexes remain constant. Overall, the summation of the delocalisation indexes involving the two metals is almost constant to 2.0 electron pairs, see Fig. 14.
- d) The Mayer bond orders do behave in a very similar way: for example, in the terminal coordination mode of $[\text{FeCo}(\text{CO})_8]^-$, the Fe–Co bond order is 0.47 and it decreases to 0.39; the 1,3 Fe...C bond order is 0.08 and it grows to 0.48 in the semibridging conformation

According to these and the above observations, the $[(\text{CO})_n\text{Co}]$, $[(\text{CO})]$ and $[\text{Fe}(\text{CO})_m]$ fragments are held together, along the whole reaction path, by four electrons distributed over three major bonding interactions (Co–Fe, Co–C, Fe–C) and many small, though

not negligible, metal–proximal carbonyl interactions. The latter are mainly responsible of the small M–M bond orders in transition metal carbonyl clusters but they do not substantially affect the evolution of the molecular graph shape along the conversion path. Instead, it is the relative amount of the three main components, strongly dependent on the θ angle, which eventually determines the abrupt changes in the molecular graph shape. In particular, the bond path linking the two metals disappears as soon as the Fe–C contribution overwhelms the Co–Fe one, as measured either by δ or by $\rho(r_b)$.

Another interesting feature revealed by this analysis is that the Fe–C bond is mainly due to metal back-donation (see Chart 3). In fact, the bp is extremely distorted at C (where donation is dominant); the dispositions of metal i-VSCCs and carbonyl VSCC look unfavourable for the donation mechanism; the large $\delta(\text{Fe},\text{O})$ delocalisation account for a dominant back-donation. We may conclude that along the terminal-to-bridging conversion, back-donation is ‘activated’ earlier and eventually the $\text{M} \rightarrow \text{C}$ electron flow overcomes the $\text{C} \rightarrow \text{M}$ one even in the symmetric bridge, as revealed by the larger negative charges and C–O distances of μ_2 carbonyls.

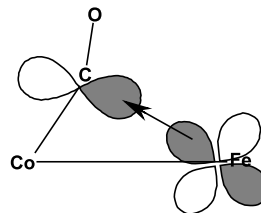


Chart 3.

3.3.6. Through bond versus through space interactions?

According to bond indexes, there is a continuum between terminal and bridging carbonyls provided that we take into account the mutual interplay of M–M, $\text{M} \cdots \text{M}$, M–C and $\text{M} \cdots \text{C}$ interactions. It is however difficult, to find a conceptual frame, within QTAM, for the 1,3 $\text{M} \cdots \text{C}$ and $\text{M} \cdots \text{M}$ interactions when their corresponding bond paths are lacking.

From an ‘orbital interaction’ point of view, one could be tempted to associate the presence of a bond path to a direct through space coupling of atomic orbitals and the significant delocalisation between two atoms not connected by a bond path to a through bond coupling mechanism [92]. However, all orbitals, molecular and basis functions, extend over the complete molecule and distant atoms ‘talk’ to one another through the mechanism of exchange (as measured by δ). Thus, to ascertain

or exclude a significant direct coupling is always rather arbitrary.³⁰

Alternatively, from a ‘valence bond’ point of view, we may think that different ‘resonant’ spin pairing structures (a few M–Cs and the M–M) contribute to the delocalised bonding in the given molecule and to the pertinent delocalisation indexes as the degree of pairing.

In both cases, we may assume that whenever two direct interactions compete, the strongest will always give rise to a bond path, while the weakest could be cancelled. In this view, the long range 1,3 M···C interaction would be definitely weak compared to M–M bond in unsupported dimers as well as the M···M interaction (compared to the M–C–M delocalisation) in bridged dimers.

3.3.7. The complete structure diagram

Recent theoretical calculations [71] on [CpNi(μ_2 -InMe)₂NiCp] (the InMe group being isolobal to CO)[93] report the presence a direct M–M bond path and a butterfly shaped molecular graph with two rings having the Ni–Ni bond path as a common edge. A similar topology was found in the experimental analysis of (CO)₃Co(μ -CO)(μ -C₄O₂H₂)Co(CO)₃ [94]. Both derivatives are ‘isoelectronic’ and structurally related to the C_{2v} isomer of Co₂(CO)₈, though their geometry are somewhat ‘distorted’ with respect to the ‘parent’ compound. In CpNi(μ -InCH₃)₂NiCp the μ -InCH₃ ligand has a significantly weaker interaction than μ -CO, accordingly, it lies much further from the metals. On the other hand, μ -C₄O₂H₂ in (CO)₃Co(μ -CO)(μ -C₄O₂H₂)Co(CO)₃ induces a compression of the Co–Co distance, which is 0.1 Å shorter than in Co₂(CO)₈. Because both a stretching of the bridging ligand and a compression of the metal–metal bond make the ring structure (with a M–M bp) more stable, the bonding picture drawn above requires an extensive analysis in a wider part of the conformational space.

Exploration of the potential energy surface of a symmetrical single-bridged dimer, namely Ni₂(CO)₇, shows that the two deformations from the equilibrium geometry (which lacks of a M–M bond path) do in fact produce a molecular graph characterised by a ring, with a M–M bp. Thus, the stability of the cyclic graph is somewhat wider if other degrees of freedom are introduced. We can somewhat reduce the multidimen-

sional structural diagram of the M–C–M system into a unified 2D picture (Fig. 15), where regions of different structural type are defined. As argued before, the boundaries separating regions of stability for each graph are bifurcation catastrophe points. In the proximity of a catastrophe point both theoretical and experimental models may be biased and subtle differences in the model may lead to substantial variation in the molecular graph. For instance, the short Co–Co distance, present in the 34-electron Co₂(η^5 -C₅H₅)₂(μ -NO)₂ dimer which was studied theoretically by Low and Hall [95], is associated with a bent Co–Co bond path at HF level but this is not confirmed when electron correlation is introduced. Similarly, calculations at B3LYP/ecp and B3LYP/ae level of theory on Co(CO)₃(μ -CO)(μ -C₄O₂H₂)Co(CO)₃ disagree with the experimental results [94], not revealing any Co–Co bond path neither in the gas-phase nor in the crystallographic geometry [96].

Extending the investigation to second transition dimers could be interesting as changes to the structural diagram may occur. Bo et al. [97] reported that the symmetrically bridged C_{2v} form of Rh₂(μ -CO)(CO)₂(H₂PCH₂PH₂)₂ has a direct Rh–Rh bp, at variance from the semibridging C_s form (where Rh–Rh distance is slightly longer). They ascribed the observed behaviour ‘to the very nature of the metal–metal interactions, a weak bent bond, and not to the method used for its analysis’ [97]. Indeed, based on the above considerations, a delocalised bonding may be hypothesised from the vanishing nature itself of the associated bp. Based on preliminary calculations [96] (at B3LYP/ecp level), Rh₂(CO)₈ in C_{2v} doubly bridged conformation show the same topology of the Co analogous, i.e. without the M–M bp. It should be noticed, however, that in Rh₂(CO)₈ the Rh–Rh distance is about 0.15 Å longer than in Rh₂(μ -CO)(CO)₂(H₂PCH₂PH₂)₂.

3.4. Small clusters

The study of dimeric species explored in the two previous sections is notable in itself, but even more important if used for the prognosis of bonding in higher nuclearity clusters, a field that received much attention by theoretical inorganic chemists. However, two aspects cannot be investigated if the analysis is restricted to bimetallic molecules: (a) the increased delocalisation occurring as the number of metals grows; and (b) the role of triply-bridging carbonyls (μ_3 -CO). The study on Co₄(CO)₁₁PPh₃ was previously used to discuss the μ_2 -CO bridging mode, and it could be also well representative of the tetrahedral stereochemistry of first and second transition group 9 clusters, characterised by a C_{3v} symmetry with a basal plane containing three μ_2 -CO bridges and an apical vertex linked through three unsupported M–M interactions (Fig. 9). However, because four-metal cages still fulfil the 18-electron rule

³⁰ Anyway, support to the significant through bond nature of the 1,3 M···C interaction comes from the analysis of the D_{3d} conformation of Co₂(CO)₈, where 1,3 Co···C delocalisation is found even with the axial carbonyls. Given the relatively large distortion of the bond path at Co (see angle β) even for those conformations where a direct Fe···C(1) is absent, the Co–C(1) interaction could be carrier of the through bond mechanism. In fact, the observed $\beta > \alpha$ can be justified only if we consider a ‘CO-insertion’ into the M–M direct coupling (a direct Fe–C(1) coupling would not affect β).

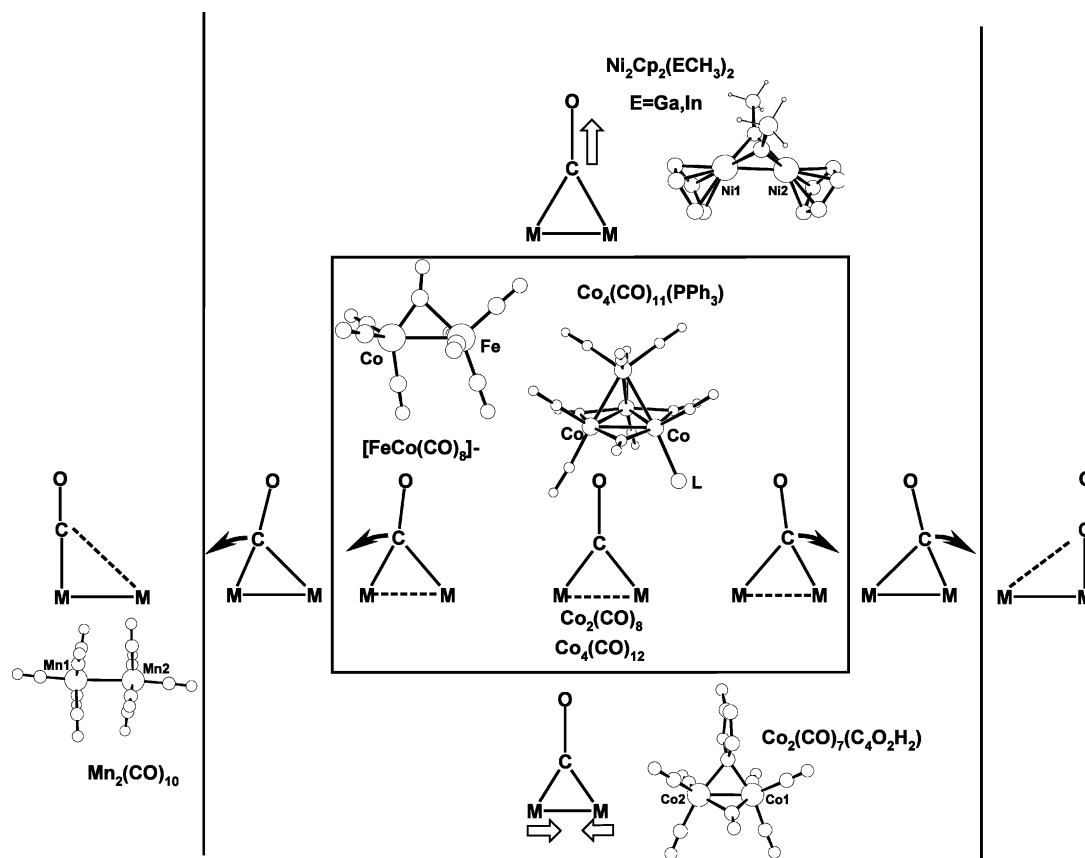


Fig. 15. Idealisation of the full conformational space for the M–C–M moiety. A solid line connecting two atoms indicates a bp linking the two atoms. A dashed line means that a direct bp is missing, though a significant delocalisation between the two atomic basins actually occurs. Regions of stability of different molecular graphs are separated by solid lines. Examples for each conformer (known from the literature) are reported. Arrays indicate deformation paths discussed in the text.

and the $M_4(CO)_{12}$ species lack of μ_3 -CO coordination, a generalisation of the metal–metal bonding in higher nuclearity clusters require further study on larger systems. Of course, the inherent complexity of both theoretical and experimental investigations grows with the molecular size, therefore symmetry may be particularly helpful. In this respect, octahedral metal clusters have to be preferred over bipyramidal pentanuclear cages, as the former may contain a crystallographic inversion centre and their idealised molecular symmetry can be even higher. For this reason, we have undertaken a systematic investigation of homoleptic, ‘isoelectronic’, octahedral cobalt clusters of general formula $[Co_6(CO)_{16-n}]^{2n-}$ ($n=0, 1, 2$; see Fig. 16). Unfortunately, isolation of the neutral species is extremely problematic [98], and all our attempts were unsuccessful so far. On the other hand, accurate electron density determinations of the two anionic species were obtained [84,99].³¹ Results are compared to those from theoretical

calculations that can give a wider perspective including the gas phase electron density of $Co_6(CO)_{16}$.

In $Co_6(CO)_{16}$, each vertex of the octahedron is linked to two terminal carbonyls. Of the eight triangular faces, four are symmetrically bridged by μ_3 carbonyls and the overall symmetry is T_d . In $[Co_6(CO)_{15}]^{2-}$, instead, the molecular symmetry is reduced to C_{3v} and we can distinguish two different basal triangular faces: metals belonging to the upper face carry one terminal, two μ_2 and one μ_3 carbonyls each; those of the opposite face have two terminal and two μ_3 carbonyls each. Of the six ‘lateral’ faces, three carry an asymmetric μ_3 -carbonyl and three are empty. Finally, $[Co_6(CO)_{14}]^{4-}$ has O_h symmetry, with six terminal carbonyls (one for each metal) along the fourfold axes and eight μ_3 carbonyls (one for each face) along the threefold axes.

A prototype molecule for describing the triply coordinated carbonyl is $[Co_3(CO)_{10}]^-$ [100].³² At the

³¹ The characterisation of the electron density on four different salts of the same anion, namely $[Co_6(CO)_{15}]^{2-}$, will allow to recognise the effects of different Madelung fields.

³² The observed X-ray conformation has a different stereochemistry, with three μ_2 -CO in the Co_3 plane. However, since we are interested in the effects of the μ_3 -CO on the M–M bond paths, we considered a $[Co_3(CO)_{10}]^-$ stereochemistry without the three double bridging carbonyls.

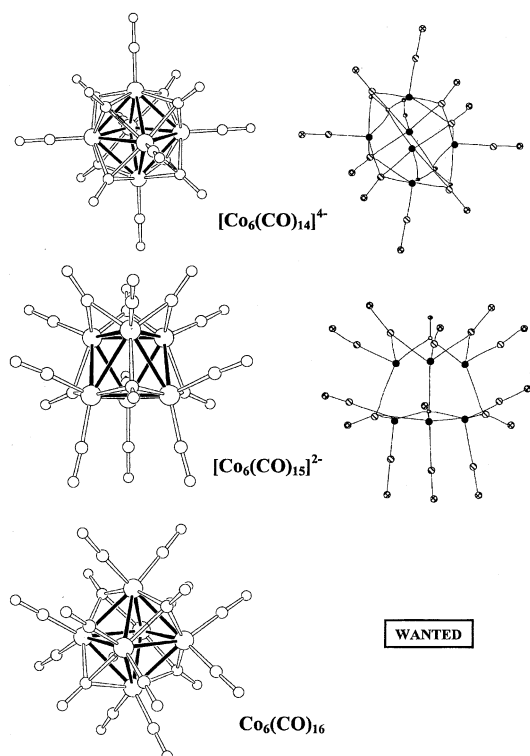


Fig. 16. Left: geometries of the $[\text{Co}_6(\text{CO})_{16-n}]^{2n-}$ ($n = 0, 1, 2$); the Co–Co edges are drawn for sake of clarifying the metal cage morphology, as it is common among metal cluster community. Right: the corresponding topologies of the electron density distribution, from experimental study; a suitable $\text{Co}_6(\text{CO})_{16}$ crystal is still wanted.

equilibrium geometry (B3LYP/ae level), the molecular graph lacks of direct metal–metal interactions and it contains three Co–C_b bond paths inwardly curved into the Co₃–C_b cone. The evolution of the electron density as CO approaches the metal ring is reported in Fig. 17. At large Co₃–CO separations, metal–metal bond paths are found with features identical to those of unsupported bonds in dimers but slightly bent out of the Co₃ plane and opposed to the incoming bridging ligand. As the CO fragment approaches the plane defined by the three metals, the M–M paths are overwhelmed by the ligand density and disappear at $d(\text{Co}_3\text{–C}_b) \sim 1.5$ Å, corresponding to $d(\text{Co–C}_b) \sim 2.20$ Å, see Fig. 17. Similarly to dimeric species, the abrupt change of the molecular graph is not reflected by sudden change of the metal–metal delocalisation indexes which are invariable close to 0.4, see Fig. 17. Other features also have a natural extension from the bi-coordination to the triply-coordination. For example, the Laplacian surrounding the bridging carbonyl is enlarged and trigonally distorted, though a unique VSCC around the carbon atom is preserved. Obviously, the longer Co–C_b distances induce smaller density at the M–C bcp's or over the interatomic surfaces and the longer C_b–O_b bond implies smaller $\rho(\mathbf{r}_{\text{bcp}})$ and a less positive Laplacian.

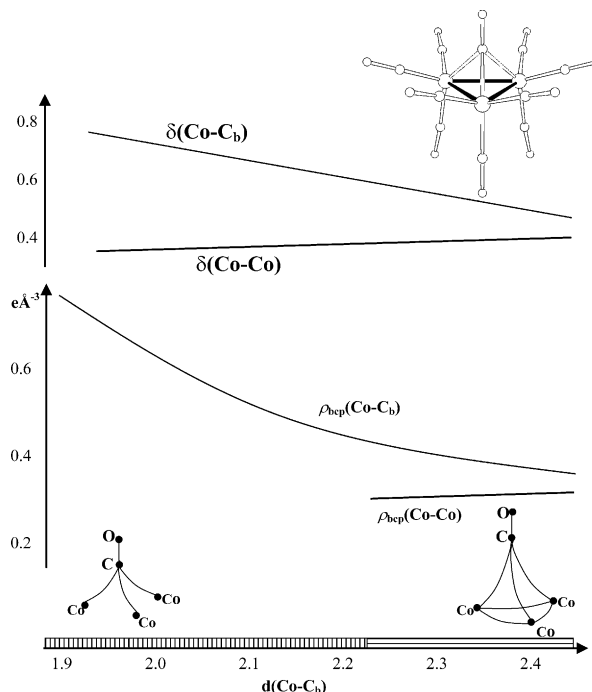


Fig. 17. Scheme representing the evolution of the electron density topology in $[\text{Co}_3(\text{CO})_{10}]^-$, as a function of the Co–C_b distance.

Having this example in mind, the absence of M–M paths in μ_3 bridged faces of $[\text{Co}_6(\text{CO})_{16-n}]^{2n-}$ species is not surprising. In fact, for first transition clusters the averaged M₃–C_b distance is 1.39 Å [87], thus shorter than the ‘critical’ 1.5 Å determined for $[\text{Co}_3(\text{CO})_{10}]^-$. In $[\text{Co}_6(\text{CO})_{14}]^{4-}$, all the eight faces are capped (with Co₃–C_b ~ 1.38 Å). Accordingly, both the experimental and the theoretical electron density display a molecular graph characterised by Co–C paths only, with 12 rcp and one ccp, see Fig. 16.

More intriguing is instead the faith of uncapped faces in polyhedral cages. In $\text{Co}_6(\text{CO})_6$ the four unsupported faces are built up by edges shared with the four triply bridged faces, therefore no M–M path is expected to occur. There is however some model dependency in our theoretical calculations and Co–Co bond paths may appear, though extremely curved inside the CO-free Co₃ faces and almost ‘collapsed’ into a rcp. Despite this ambiguity, it is reasonable considering the molecular graph as produced by 4 rcp's and one ccp without M–M bp (according to B3LYP/ae). As mentioned above, an experimental determination is unfortunately not available to confirm this model.

On the other hand, in $[\text{Co}_6(\text{CO})_{15}]^{2-}$ there are three kinds of unsupported faces. The lower basal face is defined by three Co–Co edges bearing one μ_3 -CO bridge each; the upper is instead formed by three μ_2 -CO bridged Co–Co edges; the three equivalent lateral faces have two μ_3 - and one μ_2 -bridging edges. Thus, again Co–Co bond paths are not expected, in fact they are located neither in theoretical nor in experimental

densities. The molecular graph is characterised by 5 rcp's and one ccp.

Support for the role of the M_3-C_b critical distance in determining the molecular graph topology of μ_3 bridged cages comes from the investigation of $Rh_6(CO)_{16}$. This molecule has the same stereochemistry of its Co analogous, though in second transition row clusters on average μ_3-CO lie about 1.48 Å from the metal plane. Moreover, direct M–M interactions are considered generally stronger in the second (and third) transition. As a matter of fact, theoretical calculation, on optimised and experimental $Rh_6(CO)_{16}$ geometries, show the presence of metal–metal paths, curved inside the empty faces. Their topological properties are quite similar to that of typical unsupported interactions, but for the large ellipticity measured at the bcp induced by the significant strain. A comparison with accurate experimental density could be interesting and work is currently underway.

Analysis of metal–metal delocalisation indexes in the clusters molecules here reported confirms the trend shown by dimeric complexes. In fact, even in the absence of a direct M–M bond path, the delocalisation between two metals belonging to the same face of the polyhedron is quite large ($\delta(M,M) \sim 0.35$), though less than $\delta(M,C_b)$ (~ 0.55). In addition, also the delocalisation between two opposite vertexes of the octahedron is not negligible (for example, in $Co_6(CO)_6$, $\delta = 0.03$). We may presume that as the metal cage grows, the long range M–M delocalisation becomes more significant because the number of such interactions increases. The eventual model of a metal cluster is the bulk metal itself, which is obviously dominated by such mechanism.

The charge associated with a μ_3-CO group is slightly larger than that of a μ_2-CO ligand, possibly because of a relatively stronger back-donation (each $M \cdots O_b$ delocalisation is about 0.12, hence overall $\Sigma \delta(M,O_b) \sim 0.35$). In fact, μ_3-CO have slightly longer C–O distances compared to the corresponding μ_2-CO . Additional experimental work concerning the study of intermolecular effects in the anionic clusters shows that triply bridging carbonyls have in fact more pronounced nucleophilic character [84].

3.5. Theory versus experiment

As we outlined in the previous paragraphs, there is in general a good qualitative and quantitative agreement between experimental results and theoretical predictions, which reflects the present high quality of both techniques. Nevertheless, some differences remain and they necessitate constant scrutiny through accurate analyses of the model ambiguities. In the realm of transition metal clusters, divergent results concern the topology of C–O bonds (see Section 3.1) and the presence or absence of M–M bond paths in some

bridged dimers (Section 3.3). We will briefly describe some limitations which may be at the base of the observed discrepancies.

Theoretical $\rho(\mathbf{r})$ are usually obtained from molecular orbital wave functions. They may suffer from basis set limitations (usually far from the HF quality)³³ and the neglect of electron correlation (which is difficult to introduce in dealing with large molecular systems) but they are free from experimental errors and thermal smearing. Relativistic effects are partially accounted by using ecp basis sets. Polarisation functions are vital for correct prediction of geometries and they can now be routinely introduced also for transition metal atoms [102].

On their hand, experimental electron densities use Slater orbitals, from atomic HF wave functions, and implicitly model the electron correlation, though the flexibility of the deformation functions used can hardly exceed the hexadecapolar level. The radial deformation density is limited to single ζ functions or a single contractions of HF orbitals. Usage of double- ζ functions have been reported, with significant improvement in the quality of the derived properties [13,103], though for complex systems extending the parameterisation may cause divergent refinements. Recently, much effort has been devoted also to refine first-order density matrixes, constrained to reproduce the measured intensities [104], thus resetting the experiment electron density to the same advantages and limitations of the theoretical calculations (with periodic boundary conditions). The only way to obtain experimental densities and Laplacian distributions unbiased [105]³⁴ by the choice of the radial functions would be the usage of maximum entropy methods [106],³⁵ although the most recent attitude is using this approach as a tool for improving a pre-existent (multipolar) model [107]. Relativistic effects can be introduced by using (for the core density) functions fitted to the Dirac–Fock atomic wave function [15].

For many reasons, experimental and theoretical methods can be considered as complementary, therefore their coupling could produce a wider and more detailed information. Undoubtedly, molecular geometries obtained from X-ray diffraction are the ‘reference’ for all

³³ In Ref. [39b], significantly qualitative differences were obtained when single- ζ or double- ζ Slater orbitals are used instead of the full HF expansion of Clementi and Roetti. Moreover, the usage of pseudopotentials lead to relevant discrepancies when correct Laplacian distributions are compared [101].

³⁴ In principle, the exact $\rho(\mathbf{r})$ and $\nabla^2\rho(\mathbf{r})$ should be available through Fourier summation, but series termination contaminates $\rho(\mathbf{r})$ and more heavily $\nabla^2\rho(\mathbf{r})$.

³⁵ $\nabla^2\rho(\mathbf{r})$ calculated from MEM have been reported.

theoretical calculations.³⁶ Indeed, accurate crystallography not only gives (quite rapidly) ‘exact’ molecular structures, but implicitly it provides also an analysis of the potential energy surface. The drawback is that suitable crystals must be produced. Moreover, some isomers identified in the gas phase may not be ‘frozen’ in the solid state or conformations may be severely perturbed by the crystal environment.

So far, electronic ‘excited’ states have been considered available only theoretically and not a matter of single crystal X-ray diffraction. However, although the electron density mapping is yet far from the accuracy of conventional ground state studies (especially because of the short life-times of the species), much progress has been reported in this field [108]. A very recent example, dealing with a Pt dimer, shows a significant M–M shortening upon laser excitation [109], in agreement with the theoretically predicted electron promotion from a M–M anti-bonding into a weakly M–M bonding orbital.

In order to retrieve important information on the chemical bonding, theoretical calculations are extremely useful. In fact, non-stable conformations may be studied, thus allowing investigation of the changes in electron density distribution along a given transformation (see the example reported in Section 3.3). Moreover, simple prototype models can be easily constructed and used as reference for the actual molecules. Quantities like delocalisation indexes, widely used in the previous paragraphs, can only be computed from the wave function.

4. Toward a general understanding of metal–metal interactions

Regardless of their actual disposition in the periodic table, metals are always characterised by diffuse valence density (of their *ns* electrons), which is the main cause of the observed low concentration of electrons in the bonding region even for binary (covalent) dimers formed by two (open shell) alkaline metals. For this reason, the universal indicator of charge concentration, $\nabla^2\rho(\mathbf{r})$, might be deceptive because close to zero (and therefore quite indeterminate). On the contrary, $\delta(\mathbf{A},\mathbf{B})$, the amount of electron sharing, is close to the formal bond order and $H(\mathbf{r})$ is negative as in classical covalent

bonds (although to a smaller extent), see features summarised in Table 4.

These features are found also in molecules containing bonds between transition metals. Compared to alkaline gas phase dimer, unsupported transition metal dimers are characterised by a reasonably larger electron density either at the M–M bcp and on the whole M–M interatomic surface. In fact, the *s* orbital of a transition metal is more contracted than that of a same period alkaline metal and a small d-orbital contribution may also occur. However, π -acidic ligands compete for the electron pair associated with a single M–M bond, decreasing the electron delocalisation between the two metals and annihilating the M–M bond path in some molecular conformations (bridging or semibridging CO coordination). Analysis of the principal electron sharing contributions show that no pure 2c–2e localised bonding is actually occurring even in the unsupported dimers. Instead, the system is characterised by a substantial delocalisation, mainly governed by M–M, $M\cdots M$, M–C and $M\cdots C$ interplay. The transition from one molecular graph to another is actually produced by small changes in the relative ‘weight’ of these contributions. Noteworthy, the shapes of molecular graphs are very informative because the bonding delocalisation leaves recognisable traces in the bond paths.

This tendency is particularly manifested as the size of the cage grows: the number of M–M interactions per metal (hence the delocalisation) increases and even the weaker μ_3 -coordination overwhelms the M–M bonds in triangular faces. The study of higher nuclearity clusters would be extremely informative, especially comparing electron density distribution of structural cores (where metals are linked only among each others) to that of the bulk metals themselves. Many papers reporting the electron density distributions in metals have appeared in the last decade [110]. Silvi and Gatti analysed, through periodic HF calculations, the main features of the electron density distribution and electron localisation function [75] in some metals. This allowed the visualisation of the large delocalisation which characterise the metallic bond [110]. The recent availability of experimentally refined wave functions allows such characterisation also from X-ray data in extended solids [111].

As the experimental techniques are improving at a rapid rate, the frontier of suitability is moving toward lower values of *s* (Eq. (10)) and we may expect second row transition metal clusters to be safely studied in the near future. Accordingly, we have started experiments on Rh clusters homologous of those reported in Section 3.4.

In this review, we have not considered multiple M–M bonds, but it is worthy to pinpoint that since these interactions are characterised by shorter M–M distances, more electron density is found at the bcp’s and

³⁶ A careful examination of the computational chemistry literature reveal that sometime X-ray geometries of poor quality are actually used as reference. It should be taken into account that experimental errors, disorder and uncorrected thermal motion effects do severely bias the published geometrical parameters. Therefore, the statement we report in the text is valid only under the condition of an accurate experiment and detailed analysis of the refined data.

Table 4
Summary of the features characterising atomic interactions

	$\rho(\mathbf{r}_{\text{bcp}})$	Position of \mathbf{r}_{bcp} with respect to the $\nabla^2\rho(\mathbf{r})$ profile along bp	$\nabla^2\rho(\mathbf{r}_{\text{bcp}})$	$G(\mathbf{r}_{\text{bcp}})/\rho(\mathbf{r}_{\text{bcp}})$	$H(\mathbf{r}_{\text{bcp}})/\rho(\mathbf{r}_{\text{bcp}})$	$\delta(\text{A,B})$	$\oint_{\text{A}\cap\text{B}}\rho(\mathbf{r})$
<i>Bonds between light atoms</i>							
Open-shell (covalent bonds; e.g. C–C, C–H, B–B)	Large	Close to a minimum	$\ll 0$	< 1	$\ll 0$	\sim Formal bond order	Large
Intermediate interactions (polar bonds, donor–acceptor bonds; e.g. C–O, H ₃ B–CO)	Large	Close to a nodal surface	0	≥ 1	$\ll 0$	$<$ Formal bond order	Large
Closed-shell (ionic bonds, hydrogen bonds, van der Waals interactions; e.g. LiF, H \cdots O, Ne \cdots Ne)	Small	Inside a flat region between the two outermost atomic shells	> 0	≥ 1	> 0	~ 0	Small
<i>Bonds between heavy atoms</i>							
Open-shell (e.g. Co–Co)	Small	Close to a maximum (due to the missing valence shell)	~ 0	< 1	< 0	\sim Formal bond order (unless bond delocalisation occurs)	Medium/ large
Donor–acceptor (e.g. Co–As)	Small	Close to a nodal surface	> 0	~ 1	< 0	$<$ Formal bond order	Medium/ large

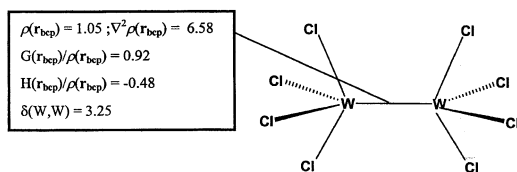


Chart 4.

on the interatomic surfaces [112]. The Laplacian is instead more positive than in single M–M, because the separation of the two metals occurs in a region which is intermediate between the atomic ns and $(n-1)d$ shells, therefore, characterised by a deeper depletion which separates two electronic shells. However, the potential energy density more consistently overcomes the kinetic energy density, while $G(\mathbf{r}_{\text{bcp}})/\rho(\mathbf{r}_{\text{bcp}})$ is larger than in M–M single bonds, see for example $(\text{W}_2\text{Cl}_8)^{2-}$ reported in Chart 4. Both these trends parallel those observed for the series C–C, C=C and C≡C (see Table 1). Moreover, the delocalisation index reflects the formal quadruple bond order (in the absence of acidic ligands). Few experimental determinations of the electron density distribution in compounds containing multiple M–M bonds have been reported so far, without complete topological analysis [113]. For this reason, new analyses within the framework of QTAM would certainly be of considerable interest.

Though weaker interactions are expected to have larger ‘uncertainties’, the agreement between theoretical calculations and experimental determinations is satisfactory even when molecular conformations are close to the boundaries of structural diagrams (i.e. catastrophe points where abrupt changes to the molecular graphs occur).

The topological analysis of the electron density distribution could be a valid tool also for rationalisation of higher nuclearity clusters, where ‘empirical’ electron counting schemes have been used so far, in the absence of sufficient predicting character from more accurate theoretical frameworks. In this respect, the technological improvements occurred during the last decade, both in computational chemistry and experimental crystallography, are promising.

Acknowledgements

We thank an ‘anonymous’ referee for very helpful and detailed suggestions and the Italian MURST (CO-FIN2000, Project ‘Metal Clusters, Basic and Functional Aspects’) for financial support.

Appendix A: List of abbreviations

bcp bond critical point

ccp	cage critical point
C _b , O _b	symmetrically bridging carbonyl
C _{sb} , O _{sb}	semibridging carbonyl
C _t , O _t	terminal carbonyl
DF	Dirac–Fock
$G(\mathbf{r})$	kinetic energy density
HF	Hartree–Fock
$H(\mathbf{r})$	total energy density
LFT	ligand field theory
M–L	metal–ligand
M–M	metal–metal
MO	molecular orbital
$P_{lm\pm}$	multipolar populations
PES	potential energy surface
Q	atomic charge
QTAM	quantum theory of atoms in molecules
Rcp	ring critical point
\mathbf{r}_{bcp}	position of the bond critical point
S	suitability index
\mathbf{S}	scattering vector
VSEPR	valence shell electron pair repulsion
X–N	X-ray–neutron deformation density
X–X	X-ray (low order)–X-ray (high order) deformation density
$y_{lm\pm}$	spherical harmonics
λ_I	eigenvalues of the Hessian matrix
$\rho(\mathbf{r})$	electron density distribution
$\nabla\rho(\mathbf{r})$	gradient of the electron density distribution
$\nabla^2\rho(\mathbf{r})$	Laplacian of the electron density distribution
$\Delta\rho(\mathbf{r})$	deformation density
$\oint_{A\cap B}\rho(\mathbf{r})$	electron density integrated over the interatomic surface separating atoms A and B

References

- [1] P. Coppens, *Science* 158 (1967) 1577.
- [2] P. Debye, *Ann. Phys.* 46 (1915) 809.
- [3] (a) B. Rees, P. Coppens, *Acta Crystallogr. Sect. B* 29 (1973) 2515;
(b) M. Iwata, Y. Saito, *Acta Crystallogr. Sect. B* 29 (1973) 8222;
(c) M. Iwata, *Acta Crystallogr. Sect. B* 33 (1977) 59.
- [4] (a) T.S. Koritsanszky, P. Coppens, *Chem. Rev.* 101 (2001) 1583;
(b) P.R. Mallinson, G. Barr, S.J. Coles, T.N.G. Row, D.D. MacNicol, S.J. Teat, K. Wozniak, *J. Synchr. Rad.* 7 (2000) 160.
- [5] (a) G. Frenking, U.J. Pidum, *Chem. Soc. Dalton Trans.* (1997) 1653;
(b) G. Frenking, N. Fröhlich, *Chem. Rev.* 100 (2000) 717 (and references therein).
- [6] R.F.W. Bader, *Atoms in Molecules. A Quantum Theory*, Cambridge University Press, Oxford, UK, 1991.
- [7] P. Coppens, P.J. Becker, *International Tables for Crystallography*, vol. C, Kluwer Academic Publisher, Dordrecht, 1995, p. 628.
- [8] J.D. Dunitz, P. Seiler, *J. Am. Chem. Soc.* 105 (1983) 7056.
- [9] K.L. Kunze, M.B. Hall, *J. Am. Chem. Soc.* 108 (1986) 5122.
- [10] (a) W.H.E. Schwarz, K. Ruedenberg, L. Mensching, *J. Am. Chem. Soc.* 111 (1989) 6926;

- (b) L. Mensching, W. Von Niessen, P. Valtanzanos, K. Ruedenberg, W.H.E. Schwarz, *J. Am. Chem. Soc.* 111 (1989) 6933.
- [11] P. Coppens, in: P. Coppens, M.B. Hall (Eds.), *Electron Distributions and the Chemical Bond*, Plenum Press, New York, 1982, p. 479.
- [12] (a) K.H. Hansen, P. Coppens, *Acta Crystallogr. Sect. A* 34 (1978) 909;
(b) R.F. Stewart, *Acta Crystallogr. Sect. A* 32 (1976) 565;
(c) F.L. Hirshfeld, *Acta Crystallogr. Sect. B* 27 (1971) 769;
(d) F.L. Hirshfeld, *Isr. J. Chem.* 16 (1977) 198, 226;
(e) B.N. Figgis, G.A. Williams, P.A. Reynolds, *J. Chem. Soc. Dalton Trans.* (1980) 2339.
- [13] B.B. Iversen, F.K. Larsen, B.N. Figgis, P.A. Reynolds, A.J. Schultz, *Acta Crystallogr. Sect. B* 52 (1996) 923.
- [14] E. Clementi, C. Roetti, *At. Data Nucl. Data Tables* 14 (1974) 177.
- [15] (a) Z. Su, P. Coppens, *Acta Crystallogr. Sect. A* 54 (1998) 646;
(b) Z. Su, P. Coppens, *Acta Crystallogr. Sect. A* 53 (1997) 749;
(c) P. Macchi, P. Coppens, *Acta Crystallogr. Sect. A* 57 (2001) 656.
- [16] E. Clementi, D.L. Raimondi, *J. Chem. Phys.* 38 (1963) 2686.
- [17] E. Elkaïm, K. Tonoka, P. Coppens, W.R. Scheidt, *Acta Crystallogr. Sect. B* 43 (1987) 457.
- [18] A. Holladay, P. Leung, P. Coppens, *Acta Crystallogr. Sect. A* 39 (1983) 377.
- [19] P. Coppens, *International Tables for Crystallography*, vol. B, Kluwer Academic Publisher, Dordrecht, 1995, p. 10.
- [20] F.K. Larsen, *Acta Crystallogr. Sect. B* 51 (1995) 468.
- [21] (a) P. Coppens, *Isr. J. Chem.* 16 (1977) 144;
(b) D. Feil, *Isr. J. Chem.* 16 (1977) 149.
- [22] (a) P. Coppens, *X-ray Charge Densities and Chemical Bonding*, Oxford University Press, Oxford, UK, 1997;
(b) V.G. Tsirelson, R.P. Ozerov, *Electron Density and Bonding in Crystals*, Inst. of Physics Publ, Bristol, 1996.
- [23] P. Macchi, Unpublished.
- [24] T. Koritsanszky, S.T. Howard, Z. Su, P.R. Mallinson, T. Richter, N.K. Hansen, *XD*, Computer Program Package for Multipole refinement and Analysis of Electron Densities from Diffraction Data, Free University of Berlin, Germany, 1999.
- [25] R.F.W. Bader, R.J. Gillespie, F. Martin, *Chem. Phys. Lett.* 290 (1998) 488.
- [26] Gaussian'98, M.J. Frisch, G.W. Trucks, H.B. Schlegel, G.E. Scuseria, M.A. Robb, J.R. Cheeseman, V.G. Zakrzewski, J.A. Montgomery, R.E. Stratmann, J.C. Burant, S. Dapprich, J.M. Millam, A.D. Daniels, K.N. Kudin, M.C. Strain, O. Farkas, J. Tomasi, V. Barone, M. Cossi, R. Cammi, B. Mennucci, C. Pomelli, C. Adamo, S. Clifford, J. Ochterski, G.A. Petersson, P.Y. Ayala, Q. Cui, K. Morokuma, D.K. Malick, A.D. Rabuck, K. Raghavachari, J.B. Foresman, J. Cioslowski, J.V. Ortiz, A.G. Baboul, B.B. Stefanov, G. Liu, A. Liashenko, P. Piskorz, I. Komaromi, R. Gomperts, R.L. Martin, D.J. Fox, T. Keith, M.A. Al-Laham, C.Y. Peng, A. Nanayakkara, C. Gonzalez, M. Challacombe, P.M.W. Gill, B. Johnson, W. Chen, M.W. Wong, J.L. Andres, C. Gonzalez, M. Head-Gordon, E.S. Replogle, J.A. Pople, Gaussian Inc., Pittsburgh, PA, 1998.
- [27] A.D. Becke, *J. Chem. Phys.* 98 (1993) 5648.
- [28] P.J. Hay, W.R. Wadt, *J. Chem. Phys.* 82 (1985) 299.
- [29] T.H. Dunning, P.J. Hay, in: H.F. Schaefer, III (Ed.), *Modern Theoretical Chemistry*, vol. 3, Plenum, New York, 1976, p. 1.
- [30] (a) A.D. McLean, G.S. Chandler, *J. Chem. Phys.* 72 (1980) 5639;
(b) R. Kryshnan, J.S. Binkley, R. Seeger, J.A. Pople, *J. Chem. Phys.* 72 (1980) 650.
- [31] A.J. Bridgeman, G. Cavigliasso, L.R. Ireland, J. Rothery, *J. Chem. Soc. Dalton Trans.* (2001) 2095.
- [32] W.L. Cao, C. Gatti, P.J. MacDougall, R.F.W. Bader, *Chem. Phys. Lett.* 141 (1987) 380.
- [33] K. Collard, G.G. Hall, *Int. J. Quantum Chem.* 12 (1977) 623.
- [34] C.K. Johnson, *ACA Abstr. Ser.* 2 29 (1992) 105.
- [35] R.F.W. Bader, *J. Phys. Chem. A* 102 (1998) 7314.
- [36] R.J. Gillespie, I. Hargittai, *The VSEPR Model of Molecular Geometry*, Allyn and Bacon, Boston, MA, 1991.
- [37] (a) R.F.W. Bader, H. Essen, *J. Chem. Phys.* 80 (1984) 1943;
(b) R.F.W. Bader, P.J. MacDougall, C.D.H. Lau, *J. Am. Chem. Soc.* 106 (1984) 1594.
- [38] (a) H. Schmider, R.P. Sagar, V.H. Smith, *J. Chem. Phys.* 94 (1991) 8627;
(b) K.D. Sen, M. Slamet, V. Sahni, *Chem. Phys. Lett.* 205 (1993) 313;
(c) R.F.W. Bader, G.L. Heard, *J. Chem. Phys.* 111 (1999) 8789 (and references therein).
- [39] (a) R.P. Sagar, A.C.T. Ku, V.H. Smith, A.M. Simas, *J. Chem. Phys.* 88 (1988) 4367;
(b) Z. Shi, R.J. Boyd, *J. Chem. Phys.* 88 (1988) 4375.
- [40] (a) A few years ago, there was a discussion about the actual effect of the so-called atomic orbital size in producing this shift, see: C.L. Perrin, *J. Am. Chem. Soc.* 113 (1991) 2865;
(b) C. Gatti, P. Fantucci, *J. Phys. Chem.* 97 (1993) 11677.
- [41] M. Otto, S.D. Lotz, G. Frenking, *Inorg. Chem.* 31 (1992) 3647.
- [42] (a) D. Cremer, E. Kraka, *Croat. Chem. Acta* 57 (1984) 1259;
(b) D. Cremer, E. Kraka, *Angew. Chem. Int. Engl. Ed.* 23 (1984) 67.
- [43] R.F.W. Bader, M.E. Stephens, *J. Am. Chem. Soc.* 97 (1975) 7391.
- [44] X. Fradera, M.A. Austen, R.F.W. Bader, *J. Phys. Chem. A* 103 (1999) 304.
- [45] J. Molina Molina, J.A. Dobado, *Theor. Chem. Acc.* 105 (2001) 328.
- [46] P.L.A. Popelier, *Atoms in Molecules: an Introduction*, Oxford University Press, Oxford, 2000.
- [47] D. Cremer, E. Kraka, in: Z.B. Maksic (Ed.), *The Concept of the Chemical Bond*, Springer-Verlag, Berlin, 1990, p. 453.
- [48] J. Molina-Molina, J.A. Dobado, L. Heard, R.F.W. Bader, M.R. Sundberg, *Theor. Chem. Acc.* 105 (2001) 365.
- [49] Y.A. Abramov, *Acta Crystallogr. Sect. A* 53 (1997) 264.
- [50] (a) V. Tsirelson, A. Stash, *Chem. Phys. Lett.* 351 (2002) 142;
(b) V.G. Tsirelson, *Acta Cryst. B* 58 (2002) 632.
- [51] F.W. Biegler-König, R.F.W. Bader, T. Ting-Hua, *J. Comput. Chem.* 3 (1982) 317.
- [52] F.W. Biegler-König, AIM2000 version 1.0, University of Applied Sciences, Bielefeld, Germany, 2001.
- [53] (a) P.L.A. Popelier, *Comp. Phys. Commun.* 93 (1996) 212;
(b) P.L.A. Popelier, *Chem. Phys.* 228 (1994) 160.
- [54] X. Girones, R. Ponc, J. Roithova, Program WBADER, 2001.
- [55] B. Rees, A. Mitschler, *J. Am. Chem. Soc.* 98 (1976) 7918.
- [56] (a) V. Jonas, G. Frenking, M.T. Reetz, *J. Am. Chem. Soc.* 116 (1994) 8741;
(b) J. Hernández-Trujillo, R.F.W. Bader, *J. Phys. Chem. A* 104 (2000) 1779.
- [57] A.J. Lupinetti, V. Jonas, W. Thiel, S.H. Strauss, G. Frenking, *Chem. Eur. J.* 5 (1999) 2573.
- [58] Y.A. Abramov, L. Brammer, W.T. Klooster, R.M. Bullock, *Inorg. Chem.* 37 (1998) 6317.
- [59] (a) R.J. Gillespie, I. Bytheway, R.S. DeWitte, R.F.W. Bader, *Inorg. Chem.* 33 (1994) 2115;
(b) I. Bytheway, R.J. Gillespie, T.-H. Tang, R.F.W. Bader, *Inorg. Chem.* 34 (1995) 2407;
(c) R.J. Gillespie, I. Bytheway, T.-H. Tang, R.F.W. Bader, *Inorg. Chem.* 35 (1996) 3954;
(d) R.J. Gillespie, *Coord. Chem. Rev.* 197 (2000) 51;
(e) R.F.W. Bader, *Coord. Chem. Rev.* 197 (2000) 71.
- [60] H.B. Davis, F.W.B. Einstein, P.J. Glavina, T. Jones, R.K. Pomeroy, P. Rushman, *Organomet.* 8 (1989) 1030.

- [61] D.A. Brown, W.J. Chambers, N.J. Fitzpatrick, R.M. Rawlson, *J. Chem. Soc. A* (1971) 720.
- [62] M. Martin, B. Rees, A. Mitschler, *Acta Crystallogr. Sect. B* 38 (1982) 6.
- [63] (a) D.A. Clemente, B. Rees, G. Bandoli, M. Cingi Biagini, B. Reiter, W.A. Herrmann, *Angew. Chem. Int. Engl. Ed.* 20 (1981) 887;
(b) D.A. Clemente, M. Cingi Biagini, B. Rees, W.A. Herrmann, *Inorg. Chem.* 21 (1982) 3741;
(c) A. Mitschler, B. Rees, M.S. Lehmann, *J. Am. Chem. Soc.* 100 (1978) 3390.
- [64] P.C. Leung, P. Coppens, *Acta Crystallogr. Sect. B* 39 (1983) 535.
- [65] (a) A.A. Low, K.L. Kunze, P.J. MacDougall, M.B. Hall, *Inorg. Chem.* 30 (1991) 1079;
(b) M.B. Hall, in: P. Coppens, M.B. Hall (Eds.), *Electron Distribution and the Chemical Bond*, Plenum Press, New York, 1982, p. 205.
- [66] W. Heijser, E.J. Baerends, P. Ros, *Discuss. Faraday Soc. (Symp.)* 14 (1980) 211.
- [67] (a) P.J. MacDougall, PhD Thesis, McMaster University, Hamilton, Canada, 1990;
(b) P.J. MacDougall, M.B. Hall, *Trans. Am. Crystallogr. Assoc.* 26 (1990) 105.
- [68] C. Bo, J.P. Sarasa, J.M. Poblet, *J. Phys. Chem.* 97 (1993) 6362.
- [69] (a) R. Bianchi, G. Gervasio, D. Marabello, *Chem. Commun.* (1998) 1535;
(b) R. Bianchi, G. Gervasio, D. Marabello, *Inorg. Chem.* 39 (2000) 2360.
- [70] P. Macchi, D.M. Proserpio, A. Sironi, *J. Am. Chem. Soc.* 120 (1998) 13429.
- [71] W. Uhl, S. Melle, G. Frenking, M. Hartmann, *Inorg. Chem.* 40 (2001) 750.
- [72] R.F.W. Bader, C.F. Matta, *Inorg. Chem.* 40 (2001) 5603.
- [73] A clear analysis of different bonding contributions in H_2 and Li_2 was presented by: W. Kutzelnigg, in: Z.B. Maksic (Ed.), *The Concept of the Chemical Bond*, Springer-Verlag, Berlin, 1990, p. 1.
- [74] G. Jansen, M. Schubart, B. Findeis, L.H. Gade, I.J. Scowen, M. McPartlin, *J. Am. Chem. Soc.* 120 (1998) 7239.
- [75] A.D. Becke, K.E. Edgecombe, *J. Chem. Phys.* 92 (1990) 5397.
- [76] F.A. Cotton, J.M. Troup, *J. Chem. Soc. Dalton Trans.* (1974) 800.
- [77] J.P. Kenny, R.B. King, H.F. Schaefer, III, *Inorg. Chem.* 40 (2001) 900.
- [78] G. Aullón, S. Alvarez, *Eur. J. Inorg. Chem.* (2001) 3031.
- [79] C.W. Bauschlicher, *J. Chem. Phys.* 84 (1986) 872.
- [80] L. Pauling, Z.S. Herman, *J. Chem. Educ.* 61 (1984) 582.
- [81] C. Mealli, D.M. Proserpio, *J. Organomet. Chem.* 386 (1990) 203.
- [82] R.H. Summerville, R. Hoffmann, *J. Am. Chem. Soc.* 101 (1979) 3821.
- [83] See for example discussion and references in: P. Macchi, D.M. Proserpio, A. Sironi, *J. Am. Chem. Soc.* 120 (1998) 1447.
- [84] (a) P. Macchi, L. Garlaschelli, A. Sironi, XX European Crystallographic Meeting, Cracow, Poland, 2001;
(b) P. Macchi, A. Sironi, Manuscript in preparation.
- [85] P. Macchi, L. Garlaschelli, S. Martinengo, A. Sironi, *J. Am. Chem. Soc.* 121 (1999) 10428.
- [86] L.J. Farrugia, D. Braga, F. Grepioni, *J. Organomet. Chem.* 573 (1999) 60.
- [87] Cambridge Crystallographic Data Centre, June 2001.
- [88] A similar correlation plot was reported previously by: A.G. Orpen, *Chem. Soc. Rev.* 22 (1993) 191.
- [89] H.B. Chin, M.B. Smith, R.D. Wilson, R. Bau, *J. Am. Chem. Soc.* 96 (1974) 5285.
- [90] (a) W. Petz, F. Weller, *Z. Kristallogr. New Crystal Struct.* 212 (1997) 157;
(b) N.K. Bhattacharyya, T.J. Coffy, W. Quintana, T.A. Salupo, J.C. Bricker, T.B. Shay, M. Payne, S.G. Shore, *Organometallics* 9 (1990) 2368;
(c) J.M. Cassidy, K.H. Whitmire, G.J. Long, *J. Organomet. Chem.* 427 (1992) 355;
(d) T.M. Bockman, H.-C. Cho, J.K. Kochi, *Organometallics* 14 (1995) 5221;
(e) B. Neumuller, W. Petz, *Organometallics* 20 (2001) 163.
- [91] P. Macchi, L. Garlaschelli, A. Sironi, *J. Am. Chem. Soc.* (2002) in press.
- [92] R. Hoffmann, *Acc. Chem. Res.* 4 (1971) 1.
- [93] W. Uhl, M. Pohlmann, R. Wartchow, *Angew. Chem. Int. Engl. Ed.* 37 (1998) 961.
- [94] (a) R. Bianchi, G. Gervasio, D. Marabello, *Helv. Chim. Acta* 84 (2001) 722;
(b) R. Bianchi, G. Gervasio, D. Marabello, *Acta Crystallogr. Sect. B* 57 (2001) 638.
- [95] A.A. Low, M.B. Hall, *Inorg. Chem.* 32 (1993) 3880.
- [96] P. Macchi, A. Sironi, Unpublished calculations.
- [97] C. Bo, M. Costas, J.M. Poblet, M.M. Rohmer, M. Benard, *Inorg. Chem.* 35 (1996) 3298.
- [98] V. Albano, P. Chini, V. Scatturin, *Chem. Commun.* (1968) 163.
- [99] (a) We have determined the accurate electron density of $[Co_6(CO)_{14}[K]_4[H_2O]_6]$, original crystal structure $[Co_6(CO)_{15}[Rb]_2]$; $[Co_6(CO)_{15}[Cs]_2[H_2O]_3]$; V. Albano, P. Bellon, P. Chini, V. Scatturin, *J. Organomet. Chem.* 16 (1969) 461;
(b) Original crystal structure $[Co_6(CO)_{15}[K]_2[H_2O]_3]$; $[Co_6(CO)_{15}[PPh_4]_2]$; V. Albano, P. Chini, V. Scatturin, *J. Organomet. Chem.* 15 (1968) 423.
- [100] H.N. Adams, G. Fachinetti, J. Strahle, *Angew. Chem.* 19 (1980) 404.
- [101] M. Kohout, A. Savin, H. Preuss, *J. Chem. Phys.* 95 (1991) 1928.
- [102] W.A. Ehlers, M. Böhme, S. Dapprich, A. Gobbi, A. Höllwarth, V. Jonas, K.F. Köhler, R. Stegmann, A. Veldkamp, G. Frenking, *Chem. Phys. Lett.* 208 (1993) 111.
- [103] A. Volkov, P. Coppens, *Acta Crystallogr. Sect. A* 57 (2001) 395.
- [104] (a) D. Jayatilaka, D.J. Grimwood, *Acta Crystallogr. Sect. A* 57 (2001) 76 (and references therein);
(b) For applications, see: D.J. Grimwood, D. Jayatilaka, *Acta Crystallogr. Sect. A* 57 (2001) 87.
- [105] (a) R.F. Stewart, in: A.G. Jeffrey, J.F. Piniella (Eds.), *The Application of Charge Density Research to Chemistry and Drug Design*, Plenum Press, New York, 1991;
(b) R.F. Stewart, *Chem. Phys. Lett.* 65 (1979) 335.
- [106] B.B. Iversen, F.K. Larsen, M. Souhassou, M. Takata, *Acta Crystallogr. Sect. B* 51 (1995) 580.
- [107] P. Roversi, XXXI Italian Crystallographic Association Meeting, Parma, Italy, 2001.
- [108] M.D. Carducci, M.R. Pressprich, P. Coppens, *J. Am. Chem. Soc.* 119 (1997) 2669.
- [109] C.D. Kim, S. Pillet, G. Wu, W.K. Fullagar, P. Coppens, *Acta Crystallogr. Sect. A* 58 (2002) 133.
- [110] B. Silvi, C. Gatti, *J. Phys. Chem. A* 104 (2000) 947 (and references therein).
- [111] D. Jayatilaka, *Phys. Rev. Lett.* 80 (1998) 798.
- [112] A. Sierralta, *Chem. Phys. Lett.* 227 (1994) 557.
- [113] A notable example is Cr–Cr quadruple bond in tetrakis(μ -oxy-6-methylpyridine)dichromium, see: M. Benard, P. Coppens, M.L. DeLucia, E.D. Stevens, *Inorg. Chem.* 19 (1980) 1924.